The Pennsylvania State University

The Graduate School

College of Engineering

TRAILING EDGE NOISE PREDICTION USING THE NON-LINEAR DISTURBANCE EQUATIONS

A Thesis in

Aerospace Engineering

by

Abhishek Jain

Submitted in Partial Fulfillment

of the Requirements

for the Degree of

Master of Science

August 2015

The thesis of Abhishek Jain was reviewed and approved* by the following:

Kenneth S. Brentner
Professor of Aerospace Engineering
Thesis Co-Advisor

Philip J. Morris
Boeing A/D Weliver Professor of Aerospace Engineering
Thesis Co-Advisor

George A. Lesieutre
Professor of Aerospace Engineering
Head of the Department of Aerospace Engineering

*Signatures are on file in the Graduate School.

ABSTRACT

AIRFOIL self-noise consists of five major sources. One of these identified sources is turbulent boundary layer – trailing edge (TBL-TE) noise, which is an important source of rotor and wind turbine broadband noise, and the focus of this thesis. Trailing edge noise is the result of unsteady flow interacting with the trailing edge of an airfoil or other sharp edged flow surface. The presence of the sharp trailing edge scatters the sound generated by the turbulent eddies very efficiently, especially for sources in the immediate vicinity of the edge. There is a need for accurate and computationally efficient methods to calculate the turbulent boundary layer trailing-edge (TBL-TE) noise that are not reliant on empirical data. The majority of the current semi-empirical techniques are based on measurements from symmetric NACA airfoil sections (i.e. NACA 0012). These techniques are generally not coupled with CFD solvers to obtain turbulent boundary layer data that provides pertinent parameters used in the acoustic calculations. Some methods exist that incorporate CFD solutions like Large Eddy simulations (LES) into their noise prediction algorithms. But these are prohibitively expensive and impractical for routine use. The method described in this paper is a first principles approach that aims to predict the TBL-TE noise using computational aeroacoustic (CAA) techniques without resorting to empiricism.

The prediction of trailing edge noise requires an accurate calculation of the boundary layer fluctuations in the vicinity of the trailing edge. Scales in the computational domain ranging from the small turbulent boundary layer scales to those of the long-range noise propagation need to be resolved. These data can be obtained using simulation techniques like Direct Numerical Simulation (DNS) or Large Eddy Simulation (LES). However such simulations for complete helicopters or wind turbine rotors are impractical given today's computational resources. Also, DNS becomes unrealistic for the propagation of the acoustic signal to distant observers. The method described here overcomes these limitations by using a hybrid CAA approach coupled with a flow solver based on the non-linear disturbance equations (NLDE). The overall problem is separated into component problems with the NLDE equations applied over a relatively small noise generating region i.e. approximately the last 10% of the chord or less. This makes the solution more computationally efficient than LES for the full airfoil or rotor and enables the use of the most computationally efficient methods in the required regions.

The proposed method is advantageous to helicopter and wind turbine manufacturers as it provides a tool for the prediction of rotor broadband noise at the design stage. This can also be used as a tool to reduce noise through the analysis of appropriate noise reduction devices.

TABLE OF CONTENTS

Chapter 3

NLDE Flow Solver

Chapter 4

Synthetic Eddy-Method

Chapter 5

Noise Prediction

Chapter 6

Conclusions

LIST OF FIGURES

LIST OF TABLES

List of Symbols

c   Speed of sound

CAA   Computational Aeroacoustics

DES   Detached Eddy Simulation

DNS   Direct numerical simulation

FW-H Ffowcs Williams and Hawkings (equation)

J   Jacobian of grid transformation

k   Thermal conductivity

LES   Large eddy simulation

M   Mach number

NLDE Nonlinear Disturbance Equations

μ Dynamic viscosity

ν Kinematic viscosity

p   Total pressure

q   Conserved vector of flow variables

ρ Density

R   Universal gas constant

RANS Reynolds Averaged Navier Stokes

Re_c Reynolds number based on chord length

T   Temperature

τ_{ij} Shear stress component in the uid on face i in direction j

TBL   Turbulent boundary layer

TE   Trailing edge

u   x component of velocity

v   y component of velocity

w   z component of velocity

Acknowledgments

Chapter 1

Introduction

The noise that emanates from helicopters as they operate under normal flight conditions has been a ubiquitous source of annoyance and is a concern for helicopter manufacturers and designers everywhere. The prediction and reduction of noise has proven to be a unique and challenging aspect of engineering design.

Rotorcraft noise consists of various sources. The first major type is rotor harmonic noise. This is any noise generated by the rotor systems on the aircraft. Harmonic thickness and loading noise are representative of the above and are caused by steady and unsteady aerodynamic forces. The major occurrence of these is at low to mid-range frequencies. High-speed-impulsive (HSI) and blade-vortex-interaction (BVI) noise are also categorized under rotor harmonic noise. These are all deterministic sources. When present, the impulsive HSI and BVI sources are often the dominant source of noise radiated by the rotorcraft.

Thickness noise is largely governed by the blade thickness and tip Mach number. It is generated when air is displaced when the blade passes through the air. In the transonic regime, thickness noise is dominated by low frequency content at the first few harmonics of the main rotor operational frequency. The intensity of thickness noise increases at high advancing tip Mach numbers.

Loading noise is generated by the application of the aerodynamic forces of the rotor on the fluid medium. It too consists of mainly low-frequency content. In a rotor system, thrust and drag are the dominant aerodynamic forces. Lifting forces create noise normal to the tip-path plane while pressure drag forces create noise near the tip-path plane of the rotor.

When the rotor blade operates in the transonic regime, local shocks form and propagate near the tip-path plane of the rotor and cause High-Speed-Impulsive (HSI) noise. Thinner blade sections and operation at lower tip speeds reduces the significance of this noise source.

Blade-vortex-interaction (BVI) noise is the impulsive version of the loading noise. The passage of the rotor blade in close proximity to trailing vortices from the preceding blade results in a rapid change of the blade aerodynamic loads, generating impulsive waves that are most intense out of the plane of the rotor. The intensity of BVI is driven by the wake geometry, the wake strength, and the miss distance between the rotor tip-path and the trailed wake.

The second major classification of rotorcraft noise is aperiodic broadband noise that can be caused by random loadings due to atmospheric turbulence, inflow disturbances, turbulence from blade boundary layer effects, vortex shedding, and flow separation. Broadband noise is comprised of components that may extend over a large range of frequencies. The importance of the prediction of broadband noise radiated from helicopters stems from the fact that for most helicopters, the frequency of the broadband noise falls in the range where the human ear is most sensitive. The contribution of broadband noise to the overall noise of the rotors can be substantial. There are many physical noise mechanisms of broadband noise generation in helicopter rotors. Essentially all the known mechanisms are associated with random pressure fluctuations on the blade surface.

Some of the sources of broadband noise are from turbulence ingestion, while there are airfoil self-noise mechanisms most classically described by the technical report of Brooks et al. [1]. The self-noise mechanisms produced by an airfoil in smooth, non-turbulent, subsonic inflow are categorized into five flow types. Each flow condition is examined through experimental measurements and a semi-empirical prediction method is developed.
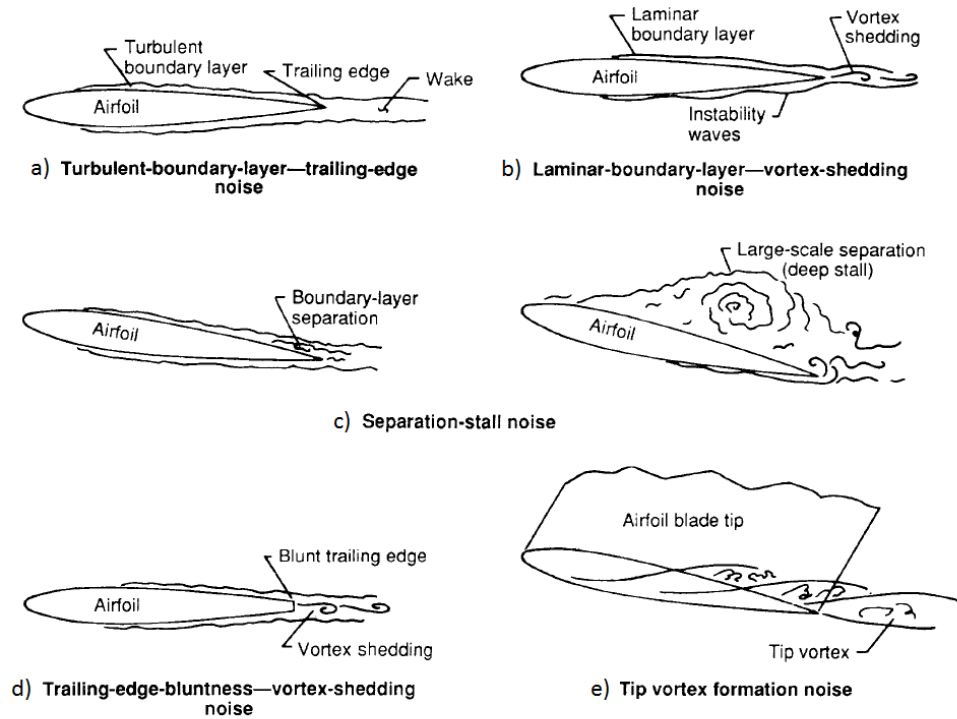
Figure 1.1: Airfoil self-noise mechanisms [1]

Airfoil self-noise occurs when an airfoil shape is placed in an otherwise uniform and steady fluid flow. Noise is generated when flow unsteadiness (in the form of fluid turbulence) interacts with the surfaces of the airfoil that generated sound. The five specific self-noise mechanisms can be listed as below

1. Turbulent Boundary Layer – Trailing Edge Noise
2. Laminar Boundary Layer – Vortex Shedding Noise.
3. Separation Stall Noise
4. Trailing Edge Bluntness – Vortex Shedding Noise
5. Tip Vortex Formation Noise.

The first of these noise mechanisms is a result of the interaction of a high Reynolds number turbulent boundary layer generated over the airfoil surface with a sharp trailing edge. Laminar boundary layers at low Reynolds number have instabilities present in the flow that cause vortex

shedding and associated noise from the trailing edge. The third noise mechanism is a low frequency phenomenon caused by large scale flow separation at high angles of attack. Pressure fluctuations caused by vorticity oscillations behind a blunt trailing edge also generate vortex-shedding noise. Lastly, the circulation of finite length blades generates tip vortex noise near the tips of the lifting blade.

1.1. Trailing Edge Noise Mechanism

The wide range of applications where trailing edge noise is a concern has resulted in an extensive array of literature available on the topic. Thus, a large effort has been put forth to understand the sound generation mechanism and the characteristics of the resulting noise. Trailing edge noise is caused by the interaction of the turbulence with a trailing edge (TE). Turbulence is characterized by the irregular flow of air and other fluids past (airfoils) or through objects (pipes, engines) and it is the usual condition of airflow considered in engineering applications. Turbulent flow can be thought of as a continuous series of randomly orientated eddies of various sizes and intensity that are linked in a form of energy cascade. This energy cascade is the physical mechanism that dissipates the energy that the immersed object imparts to the flow. Hence, turbulent flow is unsteady and contains fluctuating eddies with a large range of sizes (or scales). Fluctuating eddies by themselves are a source of noise, the most familiar form being caused by airline jet engines. The addition of a close boundary, such as an airfoil, will amplify the noise generated by fluid turbulence. Turbulent Boundary layer – trailing edge (TBL-TE) noise is also an important source of rotor broadband noise. Developing a model for accurate prediction of TBL-TE noise is an essential component of obtaining usable acoustic data.

Figure 1.2 is a diagram illustrating TE noise. On the right of the figure, the major flow processes that occur over an airfoil placed in an otherwise uniform and steady fluid stream are shown. The flow encounters the leading edge of the airfoil and forms a boundary layer due to viscosity, which that normally transitions to a turbulent state on the surface of the airfoil. Figure 1.2 illustrates the growth of this boundary layer over the airfoil surface and defines its thickness at the TE as δ. Turbulent eddies are formed within the boundary layer and it is the interaction of these eddies with the TE that generates broadband aerodynamic noise.

In acoustic terms, the edge presents itself as a sharp impedance discontinuity. This discontinuity scatters acoustic waves generated by the fluid turbulence (considered to be quadrupole) and creates an intensified radiated acoustic field. When the dimensions of the airfoil are small compared with the radiated acoustic wavelength (chord = C << λ = acoustic wavelength), then the fluctuating flow causes surface pressure fluctuations that are (effectively instantaneously) transmitted across the airfoil in the hydrodynamic near field. In this case, the radiated sound is of dipole character with the strength proportional to the fluctuating total force amplitude. This type of noise amplitude scales with the sixth power of the Mach number (M^6).

When the airfoil dimensions are large compared with the radiated acoustic wavelength (C >> λ), the TE will diffract turbulence induced quadrupole noise. In this case, the intensified radiated noise is still of a multipole nature with an amplitude governed by the intensity and spatial distribution of the turbulent field. Diffracted turbulence scales with M^5, hence for a subsonic flow (M <1) this noise is more intense that the dipole case described above.

The airfoil in Fig. 1.1 also includes TE bluntness of thickness h. The effect of bluntness is to create vortex shedding in the wake of the airfoil. This creates a stream of counter-rotating vortices with a higher spanwise (z-direction) coherency that the turbulent eddies in the turbulent boundary layer. This results in tonal noise, sometimes of dipole nature if the wavelength is smaller than the chord. The diffraction of the boundary layer turbulence, on the other hand, creates broadband noise up to high frequencies.

1.2. Motivation for present research

The Brooks, Pope and Marcolini (BPM) model was developed based on experiments with the NACA 0012 airfoil. The methods developed are semi − empirical with an analytical basis.

Using just the BPM model one is not able to obtain accurate results for different kinds of airfoils. The NAFNoise [2] code developed by the National Renewable Energy Laboratory (NREL) tried to improve the BPM model by incorporating boundary layer prediction routines such as XFOIL[54] into the solution algorithm to obtain more accurate boundary layer properties that are used as inputs into the noise prediction empirical formulae. There were still some issues with matching the exact experimental data for different airfoils and also understanding the underlying mechanisms of the self-noise. Shortcomings were also found in the noise prediction algorithm

implemented in FAST (an NREL code for wind turbines). The absence of Doppler shift effects when predicting noise resulted in a mismatch between results generated from PSU-WOPWOP (which uses a numerical implementation of the BPM model for broadband noise) [21] and FAST for flow over a whole rotor. Some options also considered were the aerodynamic load mechanisms employed in FAST compared to those employed in PSU-WOPWOP.
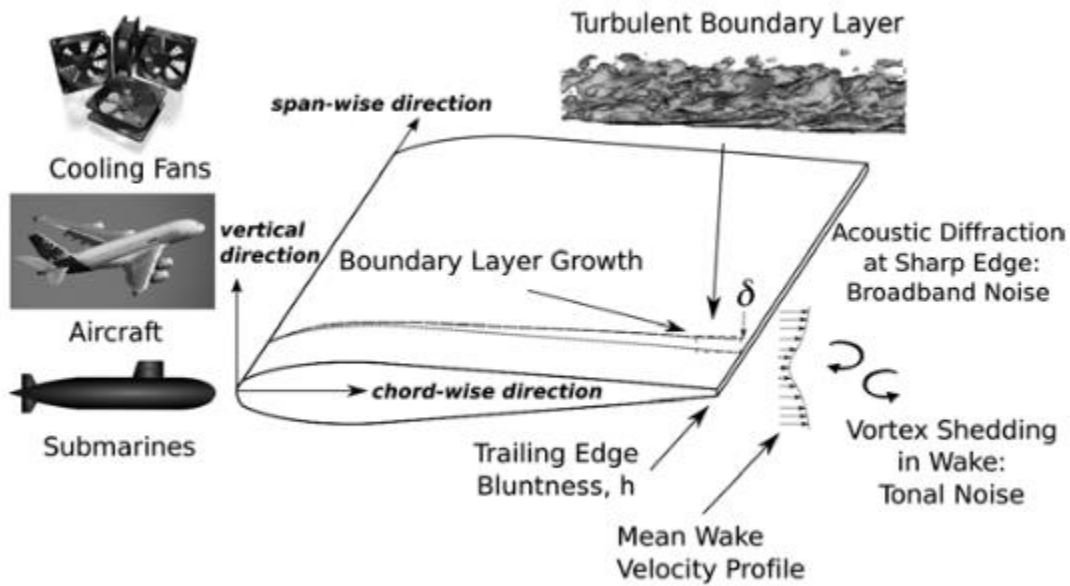
Figure 1.2: The generation of TE noise. On the left are some technologies where the TE noise limits their operation. On the right is a schematic of an airfoil, showing boundary layer growth over the surface and aerodynamic noise generation mechanisms at the TE. The turbulent boundary layer (upper right) is a computer simulation showing iso-vorticity contours of the boundary layer structure. [3]

One of the approaches to overcome this hurdle is the use of a first principles approach to obtain accurate and fast rotor broadband noise prediction. This approach involves the use of hybrid Computational Aeroacoustics (CAA).

The goal of the present project is to develop a method for accurately and efficiently calculating rotor broadband noise using a first principles approach. The present method uses a multi-level approach by dividing the entire CAA problem into components. In this manner, the most efficient computational method can be chosen to solve each component problem. Computational efficiency is also obtained by restricting the CFD domain to the trailing edge of the blade.

CHOPA, a high fidelity flow solver based on the Non- Linear Disturbance Equations (NLDE), is used to solve the CFD component of the problem and PSU- WOPWOP, a multi-functional FW-H solver, is used to solve the aeroacoustic component problem.

1.3. Organizaton of the thesis.

Chapter 2 consists of an introduction to trailing edge noise theory, the current state of prediction methods for the same and a discussion of the issues present in the various noise prediction methods including some of the problems with the Computation Fluid Dynamics (CFD) approaches to the problem.

Chapter 3 is an outline of the approach currently used in the thesis. It starts with a description of the framework and the NLDE allowing concentration on a very small portion of the domain. It also includes a description of the NLDE flow solver (CHOPA) and the techniques used (LDDRK, Unsteady dual time stepping, SEM etc.). The various inflow boundary condition techniques are also examined and the advantages and disadvantages of each are discussed.

Chapter 4 involves an explanation of the Synthetic Eddy Method (SEM), used as a turbulent inflow boundary condition, and the validation of the technique.

Chapter 5 discusses the two example cases carried out for the trailing edge noise prediction in CHOPA: a flat plate zero pressure gradient boundary layer simulation and an airfoil trailing edge noise simulation for the NACA 0012 airfoil.

Chapter 6 is a summary of the thesis and some of the additional work that needs to be performed to enhance the project.

Chapter 2

Trailing Edge Noise

Equipment used in industry today creates conditions where unsteady fluid flow and sharp edges are common. The interaction of these, both in industry and nature often creates loud and unwanted sound, which is known as trailing edge noise. The most common form of unsteady flow is turbulent, and as turbulent flow passes the trailing edge of an airfoil, strong broadband noise is generated, which can be annoying to people. Airfoil trailing edge noise can be created by wind turbines, helicopter rotors, aircraft wings, gas-turbine blades, cooling fans, propellers and submarine control surfaces. As unwanted noise reduces the quality of life and can be a public health issue, it is necessary for engineers to be able to understand, predict and control airfoil trailing edge.

2.1. Theory

Interaction with sharp edges causes a scattering of eddies present near the trailing edges. TBL-TE noise can be thought of as a scattering process, where the turbulent energy in the boundary layer fluctuations is scattered by the trailing edge and converted into acoustic energy. This results in the radiated sound intensity increasing at low freestream velocities. The sound scales with the fifth power of the flow velocity. This is in contrast to the sound intensity produced by free turbulent eddies that radiate sound intensity that scales with the eight power of the flow velocity.

The classic formulation of Ffowcs Williams and Hall [4] describes the characteristics of trailing edge noise using the inviscid form of Lighthill's equation [5]. On considering the potential field radiated by a quadrupole distribution in the vicinity of a sharp edged infinite half plane, where

the ambient fluid is at rest, it was found that the sound intensity was dependent on a relationship involving the distance between the center of an eddy and the edge of the half plane r_0, and the acoustic wavenumber k. Quadrupoles associated with eddies satisfying the inequality $2kr_0 << 1$ display sound output increase by a factor of $(kr_0)^{-3}$. Therefore, using the assumption that the acoustic wavenumber scales linearly with the characteristic fluid velocity, it was concluded that the scattered intensity increases in proportion to the fifth power of the velocity [4]. The relation for the intensity of trailing edge noise takes the form,

$$I \sim \rho_0{}^2 \; v'^2 \; \frac{U_c{}^3}{a_0} \left(\frac{L\mathcal{L}}{R^2} \right) \tag{2.1}$$

where ρ_0 is the ambient density, v'^2 is the mean square turbulent fluctuation velocity, U_c is the velocity of the convecting turbulence, a_0 is the speed of sound, L is the spanwise length of the eddies interacting with the trailing edge, $\mathcal{L}$ represents the characteristic correlation radius of the turbulent eddy and R is the separation distance of the source and the observer points. This equation is the classical formulation of trailing edge noise and is the basis of comparison for many noise prediction models and validations. Furthermore, the relation has been found to possess a directional dependence of $\sin^2(\theta/2)$ for a rigid half plane, where θ is the angle measured from the downstream direction parallel to the half plane. Comparatively, Ffowcs Williams and Hall also found that if the eddies are far enough from the edge, more specifically, if the relation $(kr_0)^{1/2} >> 1$ is satisfied, the far field sound characteristics are not amplified by the presence of the half plane edge.

Howe [6] reviewed various trailing edge noise formulations and concluded that all sharp trailing edge noise theories are essentially identical for low Mach numbers. He also presented a unified theory of trailing edge noise, investigated the effect of the Kutta condition and extended the model to include the effects of forward flight and source motion relative to the edge. These results have been validated by subsequent trailing edge noise experiments; in particular those of Brooks and Hodgson [7] on the NACA 0012 sharp edged airfoil.

2.2 Prediction methods

TBL-TE prediction methods are included in most, if not all noise prediction models. Propagation effects of the TBL-TE noise source are also important when calculating the spectra at observer locations. These usually include directivity and convective amplification effects.

Two-dimensional semi-empirical source modeling methods for airfoil self-noise prediction are most popular. Examples of these are the method developed by Brooks et al. [7] or the TNO [8] trailing edge noise prediction method. These methods discretize the rotor blade into several spanwise segments such that each segment represents a two dimensional airfoil shape. The semi-empirical models require input that is obtained using a variety of methods depending on the particular model. This ranges from using an a priori database [9] containing the necessary input data to the use of a panel integral boundary layer code [10], to a full Reynolds averaged Navier-Stokes computation to obtain the turbulent boundary layer parameters [11]. Once the source strength is found, a propagation model is used to calculate the sound pressure level for each segment at a given observer location and the element contributions are acoustically summed.

There are many challenges associated with the prediction of airfoil trailing edge noise, the most difficult of which is modeling the turbulence in the boundary layer. Exact analytical solutions are available to predict trailing edge noise (Ffowcs Williams and Hall [4], Amiet, [12], Howe [13]; however, each solution requires an estimate of the turbulent velocity or surface pressure spectrum.

The field of computational aeroacoustics (CAA) is associated with a solution of the above mentioned problem. CAA consists of a wide range of methodologies where noise is predicted through a numerical solution of the propagation of sound waves in an inhomogeneous flow field. The increase in modern day computing power has made this a popular approach in the prediction of noise. CAA consists of multiple approaches that are broadly categorized into two types. The first approach involves obtaining direct calculation of noise at an observer location by fully simulating the flow field and obtaining the acoustic pressure fluctuations. But this method is prohibitively computationally expensive. The second approach is a hybrid CAA approach which uses high fidelity CFD flow results as input to an allied aeroacoustic solver employing various acoustic analogies to determine the sound output.

Turbulence is a random, complex and highly non-linear process with no closed form solutions. Methods have been developed to resolve this issue. The methods involve varying complexities and resolution of all the scales present in turbulent flow. The most computationally demanding technique for resolving turbulent flows is Direct Numerical Simulation (DNS). DNS attempts to simulate all features of the flow, ranging from the smallest of turbulent scales to long range sound propagation when applied to the compressible Navier-Stokes equations for the acoustic field. Another technique to resolve the energy carrying eddies of the flow is called as Large Eddy Simulation (LES). LES involves the simulation of the large, energy carrying eddies of the flow and includes equations to model the small, dissipative scale eddies. The basis of LES is spatial filtering, rather than time-averaging as is popular in Reynolds Averaged Navier Stokes (RANS) methods. Spatial filtering has the consequence that turbulence scales larger than the grid size are directly resolved with no modeling assumptions. For turbulence scales smaller than the grid size, a special turbulence model is used, known as a sub-grid-scale (SGS) model. The model is transient, simulating all the fluctuations above the grid scale, therefore requiring significantly more memory than RANS, which is steady state (as the turbulence is averaged over infinite time). This method is less expensive computationally, when compared to DNS but is still intractable for large scale and frequent industrial usage. Figure 2.1 shows the associated energy spectrum that is the basis of the LES method. There have also been attempts to couple turbulence and TE noise calculations [14] to reduce computational expense by modeling aspects of turbulence using an eddy viscosity model. These methods have not proved successful when predicting high frequency noise components. Accounting for these components is important as these are the most annoying to the human ear and are heavily weighted in aircraft and other noise regulations.
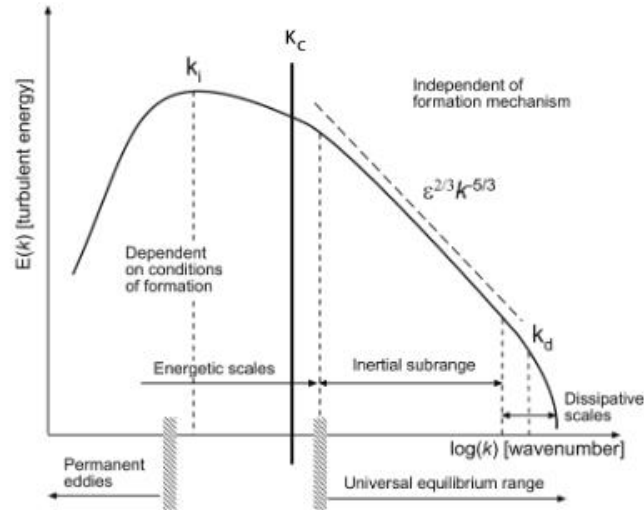
Figure 2.1: Turbulent Kinetic Energy subdivided into 3 regions. An energy containing part, a region that tranfers energy to the smaller scales and a dissipation region (LES models the energetic scales)

Another formulation that has been tried to predict turbulent trailing edge noise is the use of Unsteady RANS (URANS). RANS methods are the most widely used techniques in the industry today and are the least computationally demanding method available. The RANS method is characterized by turbulence closure models to model all the turbulent fluctuations. For application in aeroacosutics this method has some shortcomings. Detailed information about the small fluctuations are often required in aeroacoustics. However as already was mentioned, it is possible to reconstruct noise sources or recreate the stochastic turbulence field from a RANS simulation. Such techniques use a model to synthesize a turbulence field based on these time-averaged turbulence quantities [14]. There have been a number of model turbulence spectrums developed over the years from experimental velocity correlations. These model spectra use the turbulence length scales calculated by the RANS model. Once the spectral information has been determined, a deconvolution procedure is used to synthesize the transient velocity field at each point required by the noise prediction model.

Hybrid methods that are in the middle ground regarding complexity and computing power have also been tried when modeling trailing edge noise. These involve the blending between the statistical RANS and LES methods. The basis for these is to solve the boundary layer with RANS, and use LES for the external flow and separated flow region. Sometimes zonal hybrid methods are employed where a region in the vicinity of the wall is defined where the turbulent

boundary layer is solved. Communication to the outer LES regions is prescribed by an explicit boundary condition. On the other hand, in the blended hybrid methods a smooth transition is made between different regions. The most common type of a hybrid RAN-LES technique is Detached Eddy Simulation (DES) which was first proposed by Spalart and Allmaras in 1992 [15]. The general idea behind this model is that it acts as a RANS model in attached boundary layers and turns into LES for the separated flow regions. The switching between the two models depends on the local grid resolution. DES however suffers from transition layers from the interface treatment and as a result under predicts the skin friction. Methods like Delayed Detached Eddy simulation (DDES) have been developed to alleviate some of the problems encountered in traditional Detached Eddy Simulation approaches [16]. Figure 2.2 gives an account of the different grid types encountered during the application of the DES method.
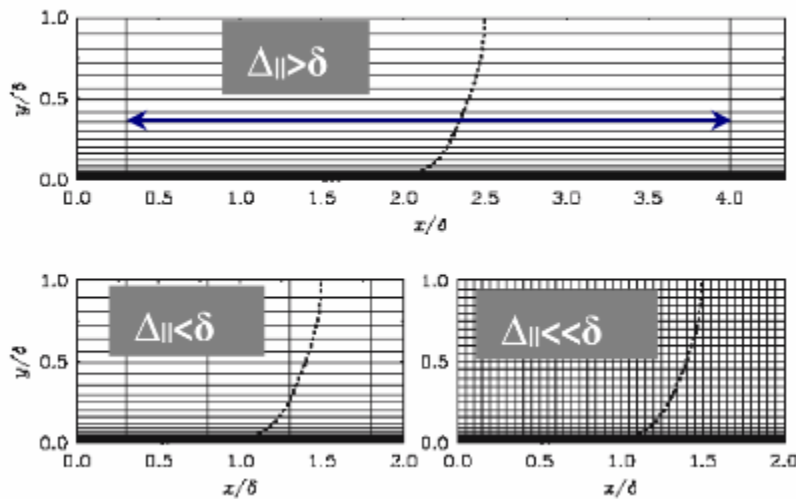
Figure 2.2: Different mesh designs as can be encountered during grid refinement in the course of DES. The first has spacing as large as the boundary layer. The second mesh has a smaller spacing than the boundary layer, but is too coarse to support LES content. The last mesh is an LES grid. [16]

Hybrid computational aeroacoustics (CAA) is the other practice adopted when trying to predict trailing edge noise. Two tools are incorporated in this approach; the first is a time dependent, high fidelity Computational Fluid Dynamics (CFD) code capable of resolving both the small and large scales of interest present in the problem at hand. The second tool required is an aeroacoustics solver based on Lighthill's acoustic analogy. In most cases the aeroacoustics code

solves the Ffowcs Williams -- Hawkings equation, which is a generalized integral formulation of Lighthill's acoustic analogy. The idea behind this approach is to obtain a full resolution of the flow variable fluctuations in the flow field surrounding the acoustic sources using the CFD solver. Then, the time dependent flow data is saved to a surface that surrounds the acoustic source and passed to the aeroacoustics solver to determine the propagation of the resulting noise.

The hybrid CAA approach is general, and only requires the ambient flow conditions, the blade geometry and the desired observer locations for input. The noise prediction is purely computational and no empirical relations are used. Therefore, provided that the CFD computation is accurate, the model can capture the resulting noise spectrum. Among other advantages is the inclusion of rotational and three-dimensional effects present on the complete, 3-dimensional rotor blade and a fully time dependent solution capable of yielding a pressure time history of the acoustic fluctuations. However, despite the reduction in computational resources required for a hybrid CAA simulation over a direct calculation, a highly resolved Direct Numerical Simulation (DNS) or even a Large Eddy Simulation (LES) of an entire rotor blade remains an impractical option given present computational capabilities.

2.3. New hybrid CAA noise prediction method.

A new technique has been developed at Penn State to make the problem of the prediction of trailing edge noise more tractable. This involves the separation of the CAA problems into modules and applying the most computationally efficient solution methods to the individual modules. First, a Reynolds Averaged Navier Stokes (RANS) solver is used to calculate the time averaged (mean) flow around the entire airfoil. Then, the Nonlinear Disturbance Equations (NLDE) are used to simulate the fine scales in the boundary layer near the airfoil trailing edge. This technique, developed by Morris et al. [17] is essentially LES except that it solves for perturbations about an estimate of the mean flow, in a limited region of the total flow. The unsteady surface pressures and/or unsteady flow field calculated by the NLDE are passed to the PSU-WOPWOP noise prediction code, which is used to predict the noise from the trailing edge.

The advantage of the NLDE method over traditional LES for aeroacoustic applications is that it increases the accuracy of the solution in the acoustic field and it can also establish a statistically stationary solution faster. This reduces the total computation time. In a full closure of the flow

solver, a turbulence model would be implemented to model the unresolved scales in the boundary layer. The NLDE are only used for the simulation of the flow in the trailing edge region of the airfoil. They predict both fluctuations on the airfoil surface as well as the fine-scale turbulence in the vicinity of the blade trailing edge. The NLDE can be solved in a small fraction of time relative to what would be required if the flow field for the entire blade needed to be calculated. The grids required for the NLDE calculations are finer than the grids needed for the mean flow computations. In conjunction with the permeable surface FW-H equation method, these compressible flow simulations enable the associated noise to be predicted.

The acoustic propagation tools used in CAA are only as good as the pressure data provided to them. An accurate FW-H solver such as PSU-WOPWOP will have limited use if the flow data given to it is low fidelity. Among the different types of noise sources, broadband noise is arguably most difficult to predict because it can originate from the smallest of flow scales: boundary layer turbulence on blade surfaces.

2.4. Issues related to CAA

Most of the issues encountered when performing CAA are different from conventional CFD problems. While most aerodynamics and fluid mechanics problems are steady-state (time independent) or involve low-frequency unsteadiness, aeroacoustics problems are by definition time-dependent. Listed below are most of the concerns when formulating CAA solutions for noise generation and prediction.

2.4.1. Large Spectral Bandwidth: TBL-TE noise is broadband and the spectrum is fairly wide. There is a need to resolve the high-frequency waves with extremely short wavelength. Developing finite difference algorithms that give adequate resolution for the number of points required per wavelength is an important issue.

2.4.2. Acoustic Wave/Mean Flow Disparity: There exists a large disparity in the acoustic and hydrodynamic fluctuations. Sometimes, the small magnitude of the acoustic disturbances might be smaller than any error incurred in the mean flow computation. This has led to the question of solving for the perturbations about the mean flow or to solve the full nonlinear equations to capture a very small-amplitude sound field directly. The NLDE method can be mentioned as a solution in this regard.

2.4.3. Far-field noise propagation: In most aeroacoustics problems, interest is in the sound waves radiated to the far field. This requires a solution that is uniformly valid from the source region all the way to the measurement point many acoustic wavelengths away. Because of the long propagation distance, CAA schemes must have minimal numerical dispersion and dissipation. Also, it should propagate the waves at the correct wave speeds and should be isotropic irrespective of the orientation of the computation mesh.

2.4.4. Non-reflecting boundary conditions: The finite size of the computational domain is compensated for by the application of appropriate boundary conditions on the artificial boundaries. For CAA problems these boundary conditions need to ensure the passage of acoustic and flow disturbances with minimal reflections. This is necessary to prevent contamination of the source of the noise. The difference between boundary conditions being applied to a CFD domain compared to a CAA domain lies in the fact that the acoustic waves decay very slowly and are still finite at the boundaries, whereas flow disturbances generally tend to decay away from their region of generation.

2.4.5. Multi-scale resolution: The various acoustic sources present in CAA problems have length scales very different from the acoustic wavelength. The length scale of the source region and that of the acoustic far field region can be vastly different. Numerical algorithms and methods should be implemented keeping multi-scale resolution in mind.

2.5. Basic elements of CAA numerical algorithms

To simulate an aeroacoustic phenomenon or problem computationally, the numerical algorithm must consist of several basic elements. These are,

2.5.1. Time-Accurate Marching computation scheme

A good quality time marching scheme is basic to any computational effort. For noise prediction, a time dependent solution for the propagation of sound waves is needed. As CAA solutions are generally unsteady (time-dependent), time-marching schemes are required. The solution should be calculated with a constant time-step which meets the stability criterion but also minimizes run time. Explicit schemes require that a pressure wave travel less than one grid point per time step. Because of the finite differencing method, if a pressure wave travels further than one cell, the

surrounding cells would not be able to properly influence the propagation. Therefore, the size of the grid spacing and local speed of sound strictly limit the size of the time stepping used. For a wave traveling between two grid points separated by a spacing of Δx,

$$\Delta t < \frac{\Delta x}{c + u} \qquad (2.2)$$

where c is the local speed of sound, u is the local flow velocity in the wave propagation direction, and Δt is an upper bound on the allowable time stepping in the explicit scheme. The new solver uses explicit five stage, fourth order accurate time marching. The scheme selected is a Low Dissipation and Dispersion Runge-Kutta (LDDRK) method outlined by Hu, Hussaini, and Manthey [18]. Details on the time marching scheme can be found in Section 3.2.1, where a more detailed limit on the time step size is also presented.

2.5.2. Suitably designed computational grid.

CFD and CAA solutions are highly grid dependent. High fidelity grids built around complex geometries are the cornerstone of efficient and robust simulations. For the TBL-TE case flow fields need to be highly resolved in the turbulent boundary layer region of the airfoil and blade surface to resolve time accurate turbulent structures or eddies. In the context of the work performed for this thesis, the grid resolution is decided by the size of the eddy generated by the turbulence injection techniques.

2.5.3. Low dispersion and low dissipation numerical scheme.

The propagation characteristics of waves governed by a series of partial differential equations depend on the dispersion relation in frequency and wave number space. The dispersion relation relates wave angular frequency and wave numbers of flow variables [19]. Using Fourier transforms of the governing equations, Tam and Webb developed a class of finite difference schemes known as Dispersion-Relation-Preserving (DRP) schemes. A fourth order accurate DRP scheme was selected for the NLDE code, which has better dispersion characteristics than a standard sixth order central difference grid. Details of the scheme used in the new NLDE code can be found in Section 3.2.3. Also, a Low-Dispersion and Low-Dissipation scheme was used for time integration and is discussed in Section 3.2.1.

2.5.4. An artificial damping algorithm or filtering procedure.

To obtain a high-quality numerical solution, it is necessary to eliminate the short wavelength spurious numerical waves. The spurious numerical waves can contaminate the computed solution. This can be achieved by the introduction of artificial selective damping terms in the finite difference equations. These damping terms can also help suppress numerical instabilities at the boundaries of the computational domain or at surfaces of discontinuities such as mesh-size change interfaces or solid wall surfaces. Explicit low-pass numerical filtering is used in the NLDE code to prevent the growth of high wave number modes inherent to central differencing schemes.

2.5.5. Numerical treatments for use at the boundaries of the computational domain.

Outgoing waves need to be able to pass through the boundaries of the computational domain with little to no reflection. Also, there is a need to reproduce the effects of the regions outside the computational domain. Incoming acoustic and vorticity waves or turbulence inflow needs to be generated by numerical boundary conditions. Far-field radiation conditions are given by Tam and Webb [19], which are derived from the asymptotic solutions of the linearized Euler equations. All boundaries away from a solid wall include some form of these radiation conditions, so acoustic waves leave without reflection and altering the interior solution. Solid wall viscous boundary conditions enforce a no-slip condition at the wall. In addition, an adiabatic condition enforces zero pressure and density gradient normal to the wall surface. Aeroacoustic boundary conditions are applied to only the perturbation variables in the solution because the mean flow is assumed to already satisfy the physical boundaries. Biased DRP finite differencing stencils are used to calculate flow derivatives at both the radiation and solid wall boundaries.

2.6. Compressible Higher Order Parallel Acoustic solver (CHOPA)

A flow solver [20] has been developed at Penn State over several years keeping in mind the above requirements for a high-fidelity CAA solver which solves about the perturbations of the mean flow using the NLDE method. The following chapter discusses the governing equation of the flow solver along with an account of the boundary conditions.

Chapter 3

NLDE Flow Solver

A high-fidelity flow solver based on the NLDE is used in the current method to resolve the smaller scales. This technique, first developed by Morris et al. [17] is an LES-like formulation except that it solves for the perturbations about an assumed mean flow. The estimated mean flow behaves as a source term in the perturbation form of the Navier-Stokes equations. In this way, the characteristic features of the full rotorcraft rotor flow field can be obtained and a high fidelity, time-dependent simulation can be performed in a limited region of interest.

The NLDE approach lends itself to the application of algorithms best suited for the solution of individual problems. Traditional, verified and robust computational fluid dynamic (CFD) approaches are used to simulate the mean flow and the NLDE solver is used to solve for the unsteady flow and acoustic fluctuations. An advantage to using the NLDE is that CAA boundary conditions for fluctuations about a known mean flow can be applied, resulting in a more accurate acoustic field.

The implementation of the overall solution is as follows (Figure 3.1). The RANS solution is obtained using well-established flow solvers. In the current research the Compressible High-Order Parallel Acoustics (CHOPA) [20] solver has also been used to obtain the RANS solution. The CHOPA solver was first developed as an aeroacoustic solver in the Aerospace Engineering Department at The Pennsylvania State University, and has since been extended for general turbulent flow simulations. This RANS solution is imported into the NLDE section of CHOPA. It is important to note that the NLDE grid in CHOPA can be different from the RANS grid, such that it is more appropriate to LES, and can also be restricted to a limited region of interest. Once the unsteady flow solution is found, the solution time history is saved on a prescribed permeable

acoustic data surface. Finally, by importing this data into the Ffowcs Williams--Hawkings solver, PSU-WOPWOP [21-23], the problem's acoustic information such as the sound pressure level at a given observer, can be obtained.
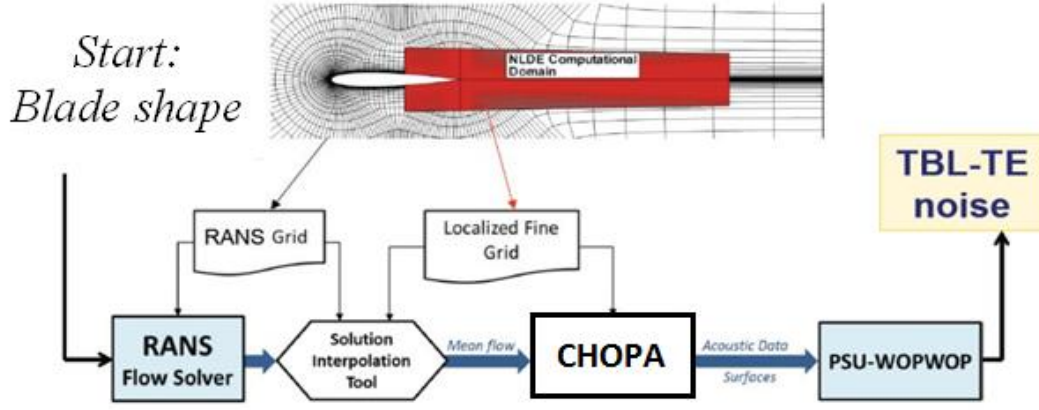
Figure 3.1: A schematic of the problem solving process. (Adapted from Christiansen et al.[24])

The flow solver has been improved for the current work by the addition of a turbulence injection boundary condition called the Synthetic Eddy method.

3.1. Governing Equations

In this section a brief summary is provided for the Non-Linear Disturbance Equations. The vector form of the three-dimensional, compressible Navier-Stokes equation:

$$\frac{dq}{dt} + \frac{dE}{dx} + \frac{dF}{dy} + \frac{dG}{dz} = \frac{dE_v}{dx} + \frac{dF_v}{dx} + \frac{dG_v}{dx} \tag{3.1}$$

where q is the conservative flow variable defined as:

$$q = \begin{Bmatrix} \rho \\ \rho u \\ \rho v \\ \rho w \\ e \end{Bmatrix}, \tag{3.2}$$

ρ is the fluid density; u, v and w are the x, y and z components of the velocity, and e is the total energy per unit volume

$$e = \frac{p}{\gamma - 1} + \frac{1}{2}\rho(u^2 + v^2 + w^2), \qquad (3.3)$$

p is the instantaneous pressure and γ is the specific heat ratio. The inviscid flux terms are:

$$E = \begin{Bmatrix} \rho u \\ \rho u^2 + p \\ \rho uv \\ \rho uw \\ (e+p)u \end{Bmatrix} \qquad (3.4)$$

$$F = \begin{Bmatrix} \rho v \\ \rho uv \\ \rho v^2 + p \\ \rho vw \\ (e+p)v \end{Bmatrix} \qquad (3.5)$$

$$G = \begin{Bmatrix} \rho w \\ \rho uw \\ \rho vw \\ \rho w^2 + p \\ (e+p)w \end{Bmatrix} \qquad (3.6)$$

and E_v, F_v and G_v are the viscous flux terms in the x, y and z directions.

After performing a long-time average and a Favre-average the instantaneous flow field is split into a time-mean part and a perturbation part q' around the time-mean values q_0.

$$q = q_0 + q' = \begin{bmatrix} \bar{\rho} \\ \bar{\rho}\tilde{e} \\ \bar{\rho}\tilde{u} \\ \bar{\rho}\tilde{v} \\ \bar{\rho}\tilde{w} \end{bmatrix} + \begin{bmatrix} \rho' \\ (\rho e)' \\ (\rho u)' \\ (\rho v)' \\ (\rho w)' \end{bmatrix} \qquad (3.7)$$

Since the time-averaged mean flow solution is known from a separate RANS computation, the Navier-Stokes equation can be rearranged to give the governing equations in terms of the disturbances. The terms involving the known time-mean quantities are treated as source terms *R(q₀)*. This rearrangement gives the NLDE as follows,

$$\frac{\partial}{\partial t}\begin{bmatrix} \rho' \\ (\rho e)' \\ (\rho u)' \\ (\rho v)' \\ (\rho w)' \end{bmatrix} + \frac{\partial}{\partial x_j}\tilde{u}_j\begin{bmatrix} \rho' \\ (\rho e)' + p' \\ (\rho u)' \\ (\rho v)' \\ (\rho w)' \end{bmatrix} + \frac{\partial}{\partial x_j}u_j''\begin{bmatrix} \bar{\rho} \\ \bar{\rho}\tilde{e} + \bar{p} \\ \bar{\rho}\tilde{u} \\ \bar{\rho}\tilde{v} \\ \bar{\rho}\tilde{w} \end{bmatrix} + \frac{\partial}{\partial x_j}\begin{bmatrix} 0 \\ 0 \\ p'_{xj} \\ p'_{yj} \\ p'_{zj} \end{bmatrix} + \frac{\partial}{\partial x_j}u_j''\begin{bmatrix} \rho' \\ (\rho e)' + p' \\ (\rho u)' \\ (\rho v)' \\ (\rho w)' \end{bmatrix}$$

$$= \frac{\partial}{\partial x_j}\begin{bmatrix} 0 \\ -q'_j + \tilde{u}_i\tau'_{ij} + u''_i\bar{\tau}_{ij} \\ \tau'_{xj} \\ \tau'_{yj} \\ \tau'_{zj} \end{bmatrix} + \frac{\partial}{\partial x_j}\begin{bmatrix} 0 \\ +u_j''\tau'_{ij} \\ 0 \\ 0 \\ 0 \end{bmatrix} + R(q_0) \qquad (3.8)$$

The u_j'' term is obtained from performing a Favre-average on the instantaneous velocity terms in the N-S equations and decomposing them into a time-averaged mean flow and perturbation part. The governing equation is integrated over time using a 5 stage 4th order low-dispersion and dissipation Runge-Kutta method.

3.2. Numerical Discretization

CHOPA is a finite difference code written in the Fortran 90 language. It is parallelized using the Message Passing Interface (MPI) for communication between processors. The spatial discretization is performed using a seven point, fourth order accurate, central difference scheme

called the Dispersion-Relation-Preserving (DRP) scheme developed by Tam and Webb [19]. The weighted coefficients used in this scheme improve the dispersion characteristics of wave propagation through the numerical domain. Near the boundary, the stencil is reduced to a fourth order central difference 5 point stencil, a 2nd order central scheme at the point adjacent to the boundary and a 2nd order one sided scheme at the boundary.

Time stepping is performed using a low dispersion dissipation 4th order Runge Kutta scheme (LDDRK). The computation time is decreased by using the dual time-stepping method and implementing Multigrid [25] and Implicit Residual Smoothing (IRS) schemes [26] during the computation. The dual time stepping scheme involves performing a series of quasi-steady computations in a fictitious time domain based on the local time step. The constraint on the physical time step, with regard to numerical stability is removed by the implementation of this technique.

3.2.1. Dispersion-Relation-Preserving Scheme (DRP)

In any CAA problem, particularly TBL-TE noise prediction, the numerical scheme needs to faithfully capture the propagation of sound waves over a long distance. Widely used finite-difference schemes inevitably cause dispersion for high-frequency wave components.

Coefficients of standard central difference schemes are derived by Taylor series expansions. They generally have the following form

$$\bar{k} \cong \frac{2}{\Delta x} \sum_{j=-N}^{N} a_j \sin k\Delta x \qquad (3.9)$$

where k is the original wavenumber and $\bar{k}$ is the modified wavenumber for the non-dispersive scheme.

These schemes do not have good dispersion conserving characteristics. Tam and Web [28] introduced a DRP scheme, wherein one free coefficient can be assigned by lowering the order of accuracy of discretization. The coefficient can be determined by minimizing the square of the difference between $k\Delta x$ and $\bar{k}\Delta x$ over the desired range of wave numbers. This guarantees a

good approximation to the original partial differential equation within the desired wavenumber range.

3.2.2. Time-Stepping schemes

Explicit Range-Kutta methods are the most popular CAA methods used to achieve high orders of accuracy. Time stepping in CHOPA is carried out using a low dispersion and dissipation 4th order Range Kutta scheme (LDDRK).

A multi-stage Runge-Kutta has the following general form:

$$\begin{cases} Q^{(1)} = Q^n \\ Q^{(2)} = Q^n + \Delta t \alpha_2 Res^{(1)} \\ \quad\quad .... \\ Q^{(K)} = Q^n + \Delta t \alpha_K Res^{(K-1)} \\ Q^{(n+1)} = Q^n + \Delta t \sum_{j=1}^{K} \beta_j Res^{(j)} \end{cases} \tag{3.10}$$

where $\sum_{j=1}^{K} \beta_j = 1$. To minimize dispersion and diffusion errors, conditions are placed on the coefficients [18]. In CHOPA, a 4th order Runge-Kutta is used for time accurate simulations with the following coefficients.

$$\propto = \left[\frac{1}{2}, \frac{1}{2}, 1\right] \tag{3.11}$$

$$\beta = \left[\frac{1}{6}, \frac{1}{3}, \frac{1}{3}, \frac{1}{6}\right] \tag{3.12}$$

These coefficients ensure good damping characteristics over a wide range of wavenumbers.

The local time step Δt is calculated in the following way, it is prescribed for various regions in the computation region

$$\Delta t = \min(\Delta t_I, \Delta t_V) \tag{3.13}$$

where Δt_I and Δt_V are the time steps due to the inviscid and the viscous contributions of the flow.

The inviscid time step Δt_I is:

$$\Delta t_I = \frac{CFL}{\lambda_\zeta + \lambda_\eta + \lambda_\xi} \tag{3.14}$$

where CFL is the Courant-Freidrichs-Lewy criterion

The Δt_V is based on the cell Reynolds number

$$\Delta t_V = \frac{\rho R_e CFL}{M\mu(|\nabla\xi|^2 + |\nabla\eta|^2 + |\nabla\zeta|^2} \tag{3.15}$$

where λ_ζ, λ_η and λ_ξ are the spectra radii of the Jacobian matrix of the flux terms in the grid transformation equation.

Explicit Runge-Kutta methods are quite efficient and easy to implement but the stability constraint puts a strict limit on the maximum allowable time step. Reduction in grid size leads to an unaffordable drop in the time step. In CHOPA, this is compensated for by using a dual time-stepping method.

3.2.3. Dual time stepping

Convergence acceleration methods have been implemented in CHOPA to overcome the low time step size that occurs due to the fine grid required to capture the turbulence and acoustic detail of the CAA problem. One of these methods is the Dual Time Stepping method, which was first introduced by Jameson [25] for unsteady flow calculations past airfoils and wings. In this algorithm a fictitious time τ is introduced to the semi-discretized equations. The governing equations are then modified as follows:

$$\frac{\partial Q}{\partial \tau} = -\frac{\partial Q}{\partial t} + Res(Q) = Res^*(Q) \tag{3.16}$$

For a dual-time stepping method, time derivatives with respect to the physical time, t, can be discretized with a three-point backward difference scheme:

$$\left[\frac{\partial Q}{\partial \tau}\right]^{n+1} = \frac{-3Q^{n,m+1} - 4Q^m + Q^{m-1}}{2\Delta t} + Res(Q^{n,m+1}) = Res^*(Q^{n,m+1}) \tag{3.17}$$

where, the index m denotes the physical time step, and the index n denotes the fictitious time step. The above discretization converts the implicit algorithm in the physical time domain to an

explicit algorithm in the fictitious time domain, which iterates to a well converged state using a four stage Runge-Kutta scheme, to ensure that the flow has reached a quasi-steady state where $Res^*(Q)$ is the predicted state residual for the next time step.

Further computational efficiency is obtained in the fictitious time domain, which is not time-accurate, using other convergence acceleration methods. Multigrid and the implicit residual smoothing method (IRS) are also available in CHOPA. The details of the implementation can be found in the CHOPA manual [27]

3.2.4. Boundary conditions

There are various boundary conditions implemented in CHOPA. The boundary conditions that are essential for use in the prediction of trailing edge noise are the following.

3.2.4.1. Non-reflecting boundary conditions.

Far-field boundary conditions are implemented on the edges of the computational domain to ensure the passage of acoustic waves as well as the flow perturbations. Tam and Webb [28] and Tam and Dong [29] developed radiation boundary conditions for this purpose by writing the instantaneous solutions as the superposition of a mean flow part and a disturbance part. Dong [29] modified these radiation boundary conditions where the mean-flow solution is not necessary. The full set of equations can be found in the CHOPA manual [27].

3.2.4.2. No-Slip Adiabatic Wall

Body surfaces are given no-slip, adiabatic wall boundary conditions. This enforces zero fluid velocity relative to the surface velocity, and zero pressure and density gradient in the direction normal to the blade surface.

3.2.4.3. Inflow boundary conditions

The restriction of the computational domain to an area of interest requires special attention to the flow data entering and leaving the boundaries. For the prediction of trailing edge noise, a detailed description of the unsteady turbulent fluctuations is only required near the trailing edge. A non-reflecting boundary condition can ensure that the outgoing waves pass out of the computational domain with minimal reflection. However, on a rotor blade, the boundary layer develops from near the leading edge, and contains fully turbulent flow by the time it nears the trailing edge. Therefore, it is important to carefully construct the turbulent fluctuations present in the developed boundary layer at the inflow boundary of a truncated domain.

3.3. Inflow Boundary Conditions

A good representation of the physical system that is being simulated is needed. Thus, the correct turbulence models need to be selected in the appropriate region of the problem. Realistic inflow boundary conditions need to be specified that are consistent with the turbulence model chosen for the particular simulation region.

The simplest inflow conditions are imposed on regions of the CFD domain where a RANS simulation is being used. Analytical and experimental profiles for the mean velocities and turbulent variables are usually imposed at the inlet of these domains. It has been shown in previous results that a universal asymptotic behavior is reached by a RANS flow irrespective of the inlet condition used.

High-fidelity techniques, on the other, hand require a more complicated specification of the inflow data. Just the application of statistical quantities, like mean mass flow rate or a mean velocity and turbulent kinetic energy profile, is insufficient for providing detailed turbulence inflow. There has to be the presence of an unsteady turbulent velocity signal representative of the turbulence at the inlet. Ideally the upstream flow would provide enough knowledge of the unsteady turbulent velocity signal but due to the limited computational domain providing the same is an unrealistic process. There are problems for which random disturbances are placed in the laminar region of the flow, but these are generally studies in which the process of transition is being studied. There is no requirement of turbulent velocity fluctuations at the inlet. In order to

limit the computational cost of the LES and DNS of spatially evolving flows, the boundaries are made to be as close to the region of interest as possible. Thus the length of the transition region that leads to true physically realizable turbulence must be made to be as short as possible.

The influence of the inlet boundary conditions on the downstream flow not only depends on the accuracy of the inflow data, but also on the flow under consideration. For free shear flows an inviscid instability mechanism amplifies exponentially the small perturbations, and the inlet boundary conditions is believed to be of small importance (Li et al., 2000 [30]) in the formation of turbulence downstream of the inlet. In contrast, for attached flows (where instability mechanisms are not so powerful), the specification of accurate boundary conditions is necessary to reach a turbulent state in the downstream flow. In all cases, it was shown by George and Davidson [31] that even simple shear flows (such as mixing layers or boundary layers) simulated with LES or DNS do not reach equilibrium states at the same location under different upstream conditions.

Several methods have been proposed to obtain turbulent fluctuations as input to the inlet of the turbulent boundary layer for unsteady compressible turbulent flows. Some of the common methods used are described below.

3.3.1. Recycling method

The concept of recycling/rescaling was first introduced by Spalart [32], simplified for incompressible flows by Lund et al. [33] and extended to compressible applications by Urbin and Knight. [34]. The technique is implemented by extracting profiles of dependent variables at some location downstream of the inflow boundary, rescaling them, and then reintroducing them at the inflow plane, in a dynamic fashion. Typically, the flow between the recycled boundaries must initially be artificially perturbed in order to generate fine-scale structures. Eventually, it will then achieve an equilibrium state. The advantage of this method is that the inflow is treated implicitly as part of the overall simulation. One disadvantage is that the rescaling is approximate. In addition, there is an imposed frequency determined by the spatial distance between the recycling boundaries. Having a greater distance between the boundaries reduces the frequency and helps

decorrelate the solution between the two. Unfortunately, this greater distance adds to the computational expense.

The design behind the formulation is to break the instantaneous flow variable into a mean and fluctuating part and rescale each part separately. The mean streamwise velocity U exhibits a two-layer behavior

$$U^{vD} = u_\tau F_i(y^+) \quad \text{Inner region} \tag{3.18}$$

$$U_\infty^{vD} - U^{vD} = u_\tau F_o(\eta) \quad \text{Outer region} \tag{3.19}$$

where $F_i(y^+)$ and $F_o(\eta)$ are dimensionless universal functions, U_∞^{vD} is the free-stream Van-Driest velocity and

$$y^+ = \frac{y u_\tau}{\nu_w} \tag{3.20}$$

$$\eta = \frac{y}{\delta} \tag{3.21}$$

where $u_\tau = \sqrt{\tau_w/\rho_w}$ is the local friction velocity, $\nu_w = \mu_w/\rho_w$ is the kinematic viscosity evaluated at the wall, δ is the local boundary layer thickness, and U^{vD} is the Van Driest transformed velocity

$$U^{vD} = \frac{U_\infty}{A} \left\{ \sin^{-1}\left[\frac{\frac{2A^2 U}{U_\infty} - B}{\sqrt{B^2 + 4A^2}} \right] + \sin^{-1}\left[\frac{B}{\sqrt{B^2 + 4A^2}} \right] \right\} \tag{3.22}$$

where

$$A = \sqrt{\frac{(\gamma - 1)}{2} Pr_t M_\infty^2 \frac{T_\infty}{T_w}} \tag{3.23}$$

$$B = \left[1 + Pr_t^{1/2} \frac{(\gamma - 1)}{2} M_\infty^2 \right] \frac{T_\infty}{T_w} - 1 \tag{3.24}$$

and $Pr_t \approx 0.89$ is the mean turbulent Prandtl number. A composite formula based on the Prandtl mixing length concept and Coles' Law of the Wake that is valid outside the viscous sublayer is

$$U^{vD} = \frac{u_\tau}{\kappa} \log_e y^+ + B' u_\tau + 2\frac{\text{II}}{\kappa} u_\tau \sin^2\left(\frac{\pi}{2}\frac{y}{\delta}\right) \tag{3.25}$$

where $\kappa = 0.4$ is Von Karman's constant, B'=5.1 and II = 0.55 (at high Reynold's numbers). Within the viscous sublayer,

$$U = u_\tau \int_0^{y^+} \left(\frac{T_w}{T}\right)^\omega dy^+ \tag{3.26}$$

where the molecular dynamic viscosity is assumed to obey

$$\frac{\mu}{\mu_w} = \left(\frac{T}{T_w}\right)^\omega \tag{3.27}$$

where ω is a constant. Eqs. 3.26 and 3.27 can be suitably blended to provide a mean streamwise velocity profile for the entire boundary layer

The fluctuating streamwise velocity component u' diplays a significant effect of compressibility. The profile of the normalized rms fluctuations $\sqrt{\overline{u'^2}}/u_\tau$ varies substantially with freestream Mach number. However, the profile of the alternatively normalized rms fluctuation $\sqrt{\bar{\rho}\overline{u'^2}/\tau_w}$ shows an approximately universal behavior for Mach numbers up to approximately five. Thus,

$$\bar{\rho}\overline{u'^2} = \tau_w I_i(y^+) \quad \text{Inner} \tag{3.28}$$

$$\bar{\rho}\overline{u'^2} = \tau_w I_o(\eta) \quad \text{Outer} \tag{3.29}$$

where I_i and I_o are universal dimensionless functions. Since $\tau_w = \rho_w u_\tau^2$, the following are obtained:

$$\overline{u'^2} = \frac{\rho_w}{\rho} u_\tau^2 I_i(y^+) \quad \text{Inner} \tag{3.30}$$

$$\overline{u'^2} = \frac{\rho_w}{\rho} u_\tau^2 I_o(\eta) \quad \text{Outer} \tag{3.31}$$

Since the mean pressure is constant across the boundary layer,

$$\frac{\rho_w}{\bar{\rho}} = \frac{T}{T_w} = \frac{T}{T_\infty}\frac{T_\infty}{T_w} \tag{3.32}$$

From 3.28 and 3.29, it therefore follows (for fixed T_w/T_∞)

$$\overline{u'^2} = u_\tau^2 \mathcal{I}_i(y^+, u_\tau/U_\infty) \quad \text{Inner region} \tag{3.33}$$

$$\overline{u'^2} = u_\tau^2 \mathcal{I}_o(\eta, u_\tau/U_\infty) \quad \text{Outer region} \tag{3.34}$$

where $\mathcal{I}_i$ and $\mathcal{I}_o$ are universal dimensionless functions.

The Strong Reynolds Analogy states that the total temperature fluctuations are negligible in non-hypersonic turbulent boundary layers at conventional rates of heat transfer. Thus, the static temperature fluctuations are to a first approximation related to the streamwise velocity fluctuations

$$T' = -\frac{1}{c_p} U u' \tag{3.35}$$

This implies that the Reynolds analogy factor R_a defined by

$$R_a = \frac{\overline{T'u'}}{\sqrt{\overline{T'^2}}\sqrt{\overline{u'^2}}} \tag{3.36}$$

is equal to unity.

Consider the mean and fluctuating flow at a location $x = x_R$ downstream of the inflow boundary (Fig. 3.2). The mean velocity components are denoted as $U_R(y)$, $V_R(y)$ and $W_R(y)$, and the mean density and temperature $R_R(y)$ and $T_R(y)$, respectively. These mean values can be obtained from the DNS or LES. Similarly, at any instant the fluctuating velocity components $u'_R(y, z, t)$, $v'_R(y, z, t)$ and $w'_R(y, z, t)$ and the fluctuating density $\rho'_R(y, z, t)$ and temperature $T'_R(y, z, t)$ can also be obtained at the recycle plane. These mean and fluctuating quantities are used to define the dynamic inflow conditions at x_I.

Lund et al. [33] developed a rescaling-recycling method for LES of incompressible turbulent flows inspired by the method Spalart and Leonard [53]. The incompressible limit of (3.18) is

$$U = u_\tau F_i(y^+) \qquad \text{Inner region} \tag{3.37}$$

$$U_\infty - U = u_\tau F_o(\eta) \quad \text{Outer region} \tag{3.38}$$

Lund et al. defined

$$\beta = \frac{u_{\tau 1}}{u_{\tau R}} \tag{3.40}$$

and since $F_i(y^+)$ and $F_o(\eta)$ are universal functions,

$$U_1(y^+) = \beta U_R(y_1^+) \qquad \text{Inner region} \tag{3.41}$$

$$U_1(\eta_1) = \beta U(\eta_1) + (1 - \beta)U_\infty \quad \text{Outer region.} \tag{3.42}$$

then Lund et al. [33] assumed

$$u_1'(y_1^+, z, t) = \beta u_R'((y_1^+, z, t) \quad \text{Inner region,} \tag{3.43}$$

$$u_1'(\eta_1, z, t) = \beta u_R'((\eta_1, z, t) \quad \text{Outer region.} \tag{3.44}$$

A similar scaling is employed for v' and w'.

Lund et al. [33] used a smoothing function $S(\eta)$ to combine the inner and outer expressions for the velocity components. For the streamwise velocity,

$$U_1 = [1 - S(\eta_1)](U_1 + u_1')|_{Inner} + S(\eta_1)(U_1 + u_1')|_{Outer}, \tag{3.45}$$

where

$$S(\eta) = f(x) = \begin{cases} \frac{1}{2}\left[1 + \tanh\left[\frac{a(\eta - b)}{(1 - 2b)\eta + b}\right][\tanh a]^{-1}\right], & \eta \le 1 \\ 1, & \eta > 1 \end{cases} , \tag{3.46}$$

and $a = 4$ and $b = 0.2$ are constants. The value of a determines the width of the regions where S transitions from zero to one, and b determines the location of the transition. A value $b = 0.2$ provides a smooth transition at $\eta \approx 0.2$

The friction velocity at the inflow is determined from the relation,

$$u_{\tau 1} = u_{\tau R} \left(\frac{\theta_R}{\theta_1}\right)^{\frac{1}{[2(n-1)]}} , \tag{3.47}$$

where θ is the incompressible momentum thickness and $n=5$.

Urbin and Knight [34] extended the method of Lund et al. to compressible turbulent boundary layers. Assuming the mean profiles at x_R are an accurate representation of the turbulent flow, the mean streamwise U_R satisfies (3.48) and (3.49)

$$U_R^{vD} = u_{\tau R} F_i(y^+) \qquad \text{Inner region,} \tag{3.48}$$

$$U_\infty^{vD} - U_R^{vD} = u_{\tau R} F_o(\eta) \qquad \text{Outer region.} \tag{3.49}$$

Since $F_i(y^+)$ and $F_o(\eta)$ are universal functions,

$$U_1^{vD}(y^+) = \beta U_R^{vD}(y_1^+) \qquad \text{Inner region,} \tag{3.50}$$

$$U_1^{vD}(\eta_1) = \beta U^{vD}(\eta_1) + (1-\beta)U_\infty^{vD} , \qquad \text{Outer region.} \tag{3.51}$$

The mean velocity U_1 is obtained from (3.50) and (3.51). For a given location y_1, the corresponding location y_n is obtained from $y_R^+ = y_1^+$ in the inner region and $\eta_1 = \eta_R$ in the outer region, thus

$$y_R = \beta y_1 \quad \text{Inner region} \tag{3.52}$$

$$y_R = \alpha y_1 \quad \text{Outer region} \tag{3.53}$$

Assuming $T_{w1} = T_{wR}$. The following empirical correlations are used,

$$\alpha = \left[1 + \frac{(x_R - x_1)}{\delta_1} 0.27^{\frac{6}{5}} Re_{\delta_1}^{\frac{-1}{5}}\right]^{\frac{-5}{6}} , \tag{3.54}$$

and

$$\beta = \epsilon^{-\frac{1}{10}} , \tag{3.55}$$

where

$$\epsilon = \frac{\delta_1}{\delta_R}.$$
(3.56)

The mean wall normal velocity is scaled in a similar manner.

The mean temperature at the inflow boundary is

$$T_1(y_1^+) = T_R(y_1^+), \quad \text{Inner region,}$$
(3.57)

$$T_1(\eta_1) = T_R(\eta_R), \quad \text{Outer region.}$$
(3.58)

The mean density is obtained from the ideal gas law $\bar{p} = R R_g T$.

Thus, as we neglect the variation of u_τ between x_I and x_R, Eq (3.52) suggests

$$u_1'(y_1^+, z, t) = \beta u_R'((y_1^+, z, t), \quad \text{Inner region,}$$
(3.59)

$$u_1'(\eta_1, z, t) = \beta u_R'((\eta_1, z, t), \quad \text{Outer region.}$$
(3.60)

And similar scaling is employed for v' and w'.

Static temperature fluctuations are assumed to scale in a simple manner

$$T'_1(y_1^+) = T'_R(y_1^+), \quad \text{Inner region,}$$
(3.61)

$$T'_1(\eta_1) = T'_R(\eta_R), \quad \text{Outer region.}$$
(3.62)

The inner and outer expressions for the mean and fluctuating velocity, density and temperature are obtained at x_R at each time step across the entire boundary layer, and combined using the smoothing function $S(\eta)$ of Lund et al. The two other inflow velocity components and temperature are generated in a similar manner. The static pressure is assumed to be constant, and the instantaneous density is computed from the ideal gas law.
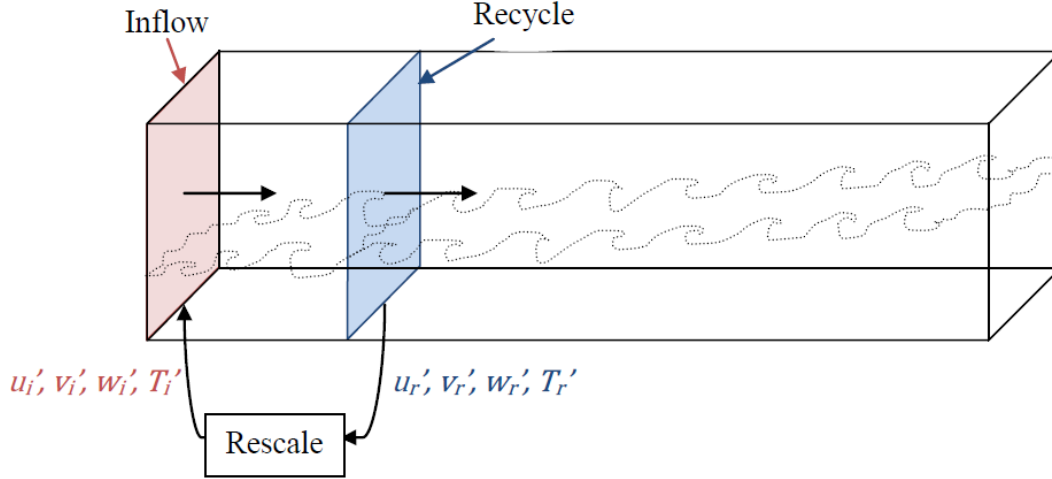
Figure 3.2: Schematic depiction of the Recycling method.

Recycling techniques based on the formulation of Urbin et al. are probably the most effective and least expensive inflow boundary conditions available to simulate a spatially evolving wall bounded flow. However these methods suffer from drawbacks. First, the simulated flow is required to be in an equilibrium state at the inlet for the scaling laws to apply. In addition,

1. The recycling procedure retains the memory of the streamwise-periodic origin of the inflow, thus introducing a spurious periodicity in the flow direction.

2. The flow initialization strongly influences the effectiveness of the method. Inappropriate initial conditions, such as white noise, might not be sustainable and can even lead to a relaminarization of the flow.

3. A precursor simulation is required to initiate the flow.

3.3.2. Precursor databases

This is a more general method to generated inflow data is to extract it from a separate precursor database. Providing an adequate scaling of the velocity fluctuations, the database can supply inflow data for a large variety of configurations and Reynolds numbers. Nonetheless, such methods require large storage capacities.

3.3.3. Synthetic Turbulence

Most of the synthetic turbulence methods generate turbulence using randomized signals. The main goal of these methods is to modify these sequences in such a way that they do not vanish under numerical or viscous dissipation and that their statistical properties are close to those of a real flow. This was first introduced by Lund et al. [33]. This method used a basic random fluctuation method, according to which target Reynolds stresses are assigned to a white noise and introduced at the inlet. The data generated by this method lacked both turbulent structure and nonlinear energy transfer. A long adaptation distance of 50 boundary layer thicknesses was needed for the transition to physical turbulence. An evolution of this method was proposed which consists of prescribing velocity fluctuations with a specified power spectrum and random phase. Together with the additional computational effort to evaluate the fast Fourier transforms, the resulting method required a relatively long spatial development for the flow to become physically realistic. Another approach followed by Mahesh et al. [35] and Na and Moin [36] was to randomize the amplitude of the Fourier modes rather than their phase. These operations were applied to a frozen turbulent DNS field to generate sequences of fluctuations, which were then superimposed on a mean velocity field. The friction coefficient was shown to recover after three boundary layer thicknesses, but the method also introduced an unphysical periodicity, which can be problematic in some applications. Another spectral-based inflow generation method is based on the work of Kraichnan [37], later adapted to an anisotropic turbulence by Smirnov et al. [38] and simplified by Battern et al. [39]. The principle is to build the fluctuation velocity field as a superposition of spatiotemporal Fourier modes with random-based amplitudes and phases. It includes the anisotropy information in the formula for the amplitude and allows for a specification of a length and time scale. This method was tested by Keating et al. [54] and led to adaptation distances of more than 20 initial boundary thicknesses. A more complex method based on the specification of autocorreleation lengths yielded adaptation distances of the order of ten boundary layer thicknesses. The last type of synthetic method gathers procedures that include a slight degree of empiricism. They are based on the idea that turbulence can be reproduced by a superposition of coherent structures with given shape, length, and time scale. Sandham et al. [40] derived a method in which turbulent structures are modeled by a sum of trigonometric functions yielding an adaptation distance of 40 displacement thicknesses. On a more realistic basis, Perry and Marusic [41] showed that the Reynolds stresses and the mean velocity profile of a turbulent

plane channel can be accurately reproduced from a superposition of analytical hairpin-type vortical structures. In the same spirit, Mathey et al. [42] chose to superimpose randomly located Guassian-shaped streamwise vortices. Jarrin et al. [43] further extended the latter methods to arbitrary-shaped vortices with prescribed second-order moments.

Compared to recycling methods, synthetic techniques have none of the three drawbacks highlighted above because they are feed forward and their random nature is expected to suppress any periodicity. Besides, a synthetic inflow condition does not need any initialization and thus reduces the initial transient mentioned above down to one flow through time. However, even complex synthesizing procedures can lead to adaptation distances of the order of $20\delta_0$. Hence, Spille-Kohoff and Kaltenbach [44] proposed to add a feedback path to the former method in order to shorten this distance, with the addition of source terms for the wall-normal velocity in the Navier–Stokes equations at given streamwise locations. The amplitude of these terms is tuned to minimize the error between the Reynolds stresses at given control planes and the Reynolds stresses specified at the inlet. This method has been applied to the synthetic condition of Batten et al. [39] and reduced the adaptation distance from 20 to 10–15 δ_0. Yet a major drawback of synthetic methods is that the statistics needed for the process (such as the mean velocity profile, the Reynolds stresses or the energy spectrum) must be known *a priori*. Most of the studies that use synthetic inflow have recourse to the statistics extracted from another simulation performed with a different inflow method. However, the approach followed here looks to overcome the issues mentioned above.

The idea followed in the present study is inspired by the work of Perry and Marusic, [41] which suggests that the injection of analytical eddy structures, whose shapes are representative of typical coherent structures of the turbulent boundary layer, provides a good approximation for the low-order statistics of such wall-bounded flows. In this regard, the method proposed by Jarrin et al., [43] known as the synthetic-eddy method referred to as SEM, can be used as a statistical tool to create turbulent structures with a given shape and prescribed Reynolds stresses. Smaller adaptation distances should probably be obtained if the SEM is fed with a realistic scale and shape distribution across the boundary layer.

The Synthetic Eddy Method is described in more detail in the next chapter.

Chapter 4

The Synthetic Eddy-Method

In order to generate physically realistic fluctuations at the inflow boundary of the NLDE domain, a modified Synthetic Eddy Method (SEM) is used. Originally formulated by Jarrin et al. [43], it was extended by Pamies et al. [45] and Roidl et al.[46] This method can be used as a statistical tool to create turbulent structures with a given shape and prescribed Reynolds stresses. Modifications have been made to this method to obtain smaller adaptation distances by providing realistic shape and length scale distributions across the boundary layer.

Shortcomings of previously used synthetic techniques, such as the need for a priori statistics as input and large adaptation distances ($\sim>10\delta_0$) were sought to be overcome by the use of the SEM.

The basis of the original SEM was to generate a velocity signal with prescribed first- and second-order moments. This operation uses the Cholesky decomposition A_{ij} of a prescribed Reynolds stress tensor R_{ij} to assign second order moments to a nomalized stochastic signal $\tilde{u}_j(x,y,z,t)$ superimposed on a mean $U_{RANS,j}(y)$ velocity distribution,

$$u_j(x,y,z,t) = U_{RANS,j}(y) + \sum_i A_{ij}u'_j(x,y,z,t), \qquad (4.1)$$

where u'_j must be a centered random sequence with unit variance and zero covariance. x, y and z are the spatial coordinates in the streamwise, wall-normal and transverse directions, respectively. The major terms of the Cholesky tensor are A_{ii} and A_{21}. The principle of SEM is then to define $\tilde{u}_j$ as a superimposition of turbulent Gaussian structures. The method is finally tuned by assigning a length scale and a convection velocity to these structures.

The modification made to the original method is the population of coherent turbulent structures as a function of distance from the wall. This then accounts for the inhomogeneity of scales. The inlet plane is split into p zones, in which SEM is applied separately with different control parameters. The random signal $\tilde{u}_j$ needed for the Cholesky decomposition is computed as a sum over the P zones.

$$\tilde{u}_j = \sum_{p=1}^{P} v_{jp} \tag{4.2}$$

where v_{jp}, which corresponds to normalized random sequences, has a compact support on the pth zone, and will be referred to as a mode.

Figure 4.1 visualizes the virtual volumes $V_{virt,p}$ around the NLDE inflow boundary based on three inflow zones ($P=3$). The virtual volumes are defined by the streamwise, the wall-normal, and the spanwise dimensions of the turbulent length-scale l_x, the height of the plane $L_{y,p}$ and the width of the computational domain L_z
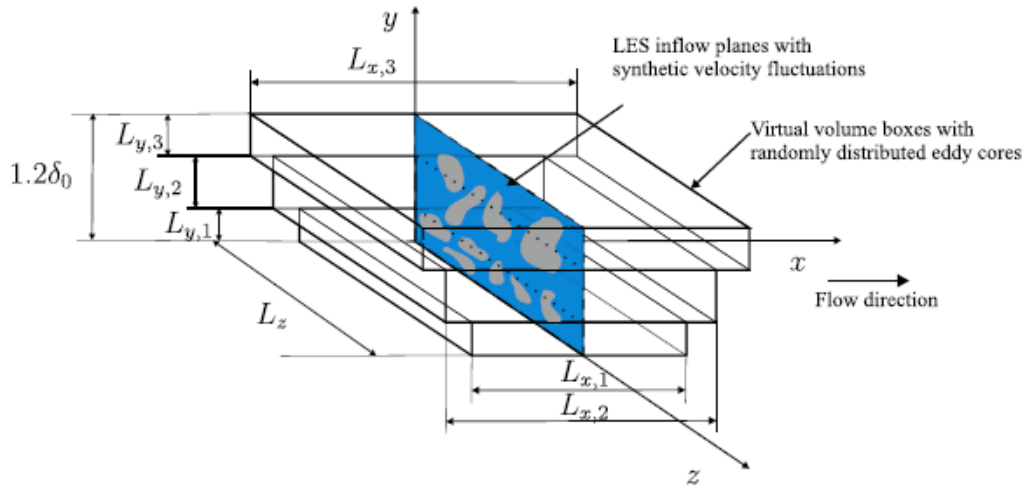

Figure 4.1: Sketch of three virtual volume boxes that encompass an LES inflow boundary on which the resulting synthetic velocity fluctuations are projected. [46]

The whole random signal $\tilde{u}_j$ is then generated according to Eq. (4.1), where each mode, v_{jp} is defined as a superimposition of $N(p)$ turbulent structures. Each structure is randomly positioned in the inlet plane using the location of its center (x^i, y^i, z^i). It is also assigned a random sign ε_j^i. These structures are characterized for each mode by a shape function $f_{l_{(x,y,z)},j,p}$, which has compact support on $[-1; 1]$, and satisfies the normalization condition,

$$\frac{1}{2^3} \int_{[-1,1]^3} \left(f_{l_x,j,p}(\tilde{x}) f_{l_y,j,p}(\tilde{y}) f_{l_z,j,p}(\tilde{z}) \right)^2 d\tilde{x}\, d\tilde{y}\, d\tilde{z} = 1 \tag{4.3}$$

To simplify the specification of the shape functions, their dependence with time and space coordinates is separated and they are expressed as a product of three one-dimensional functions $f_{l_x,j,p}(\tilde{x})$, $f_{l_y,j,p}(\tilde{y})$, and $f_{l_z,j,p}(\tilde{z})$, where $\tilde{x}$, $\tilde{y}$ and $\tilde{z}$ are the reduced variables for the streamwise, wall-normal, and transverse directions, respectively, defined below. Finally, the streamwise scale (l_p^x) as well as wall-normal (l_p^y) and transverse (l_p^z) length scales are assigned to each structure using a variable substitution,

$$u'_j(x,y,z) = \sum_{p=1}^{P} \frac{\sqrt{V_{virt,p}}}{\sqrt{N(p)}} \sum_{i=1}^{N(p)} \varepsilon_j^i f_{l_x,j,p}(\tilde{x}) f_{l_y,j,p}(y) f_{l_z,j,p}(\tilde{z}) \tag{4.4}$$

where,

$$\tilde{x} = \frac{x - x^i}{l_p^x}, \tilde{y} = \frac{y - y^i}{l_p^y} \text{ and } \tilde{z} = \frac{z - z^i}{l_p^z}$$

The virtual eddy cores convect in the streamwise direction with the velocity u_{con} (Table 4.1). To imitate the ejective motion of the eddy in the log- and outer layer a convective velocity in the wall-normal direction is prescribed by

$$v_{con} = C_{con} U_\infty \sqrt{\left| \frac{y^i - y_{min,p}}{L_{y,p}} \right|} \tag{4.5}$$

where $L_{y,p}$ is the wall-normal length scale, $y_{min,p}$ us the smallest normal distance to the wall of the plane p, and C_{con} is a constant that determines the angle of the incoming flow structures. The ejection angle of the structures depends on the flow Mach number. In supersonic boundary layers the angle is higher than in subsonic boundary layers. For subsonic and supersonic boundary

layers, the constant is chosen as $C_{con} = 0.25$ and $C_{con} = 0.5$, respectively. The new position of the eddy core at $t = t_0 + \Delta t$ is calculated from

$$x^i(t) = u_{con}\Delta t + x^i(t_0), \qquad (4.6)$$

$$y^i(t) = v_{con}\Delta t + y^i(t_0). \qquad (4.7)$$

Once $\tilde{x} > 1$ or $\tilde{y} > 1$, a new eddy core assigned with randomly chosen coordinates x^i, y^i, z^i and sign ε_j^i is generated.

The number of structures per mode $N(p)$ can be adjusted so that the support of mode p remains statistically covered by structures.

$$N(p) \approx \frac{S_p}{S_s} \qquad (4.8)$$

where S_p is the surface of a transverse plane $[S_p = L_z(y_p^{low} - y_p^{up})]$ and S_s is the transverse surface of the support of the shape function $S_s = 4l_p^y l_p^z$

4.1. Tuning the shape function for the various modes.

The modified SEM is capable of producing randomly located turbulent structures, of customizable sizes, celerity and geometrical shape. Physical arguments help to divide the boundary layer into three parts: the viscous sublayer, the logarithmic zone and the wake region. The link between the first and second zone is a transition region called the buffer layer.

Two types of scales are identified and structures are produced according to the various parameters present in these modes. For the near wall regions, scales are assumed to depend on the viscosity ν_w and the friction velocity $u_\tau = \sqrt{\dfrac{\tau_w}{\rho_w}}$ (where τ_w is the wall shear stress and ρ_w is the fluid density at the wall). Outer scales depend on the global properties of the flow; e.g., δ and U_∞. Statistical variables as well as physical scales of the near-wall region are known to be quite

universal when expressed in inner scaling. Similarly flow features in the outer part of the boundary layer are described well with outer scaling.

Plane	$L_{y,p} = [y_{min}; y_{max}]$	l_x	l_y	l_z	u_{con}	v_{con}
p=1	$[0; 60^+]$	$(100)^+$	$(20)^+$	$(60)^+$	$0.6U_\infty$	-
p=2	$[60^+; 0.65\delta_0]$	$\dfrac{36\theta}{Re_\theta^{\frac{1}{4}}}$	$\dfrac{12\theta}{Re_\theta^{\frac{1}{4}}}$	$\dfrac{15\theta}{Re_\theta^{\frac{1}{4}}}$	$0.75U_\infty$	Eq. (4.5)
p=3	$[0.65\delta_0; 1.2\delta_0]$	$\dfrac{50\theta}{Re_\theta^{\frac{1}{4}}}$	$\dfrac{20\theta}{Re_\theta^{\frac{1}{4}}}$	$\dfrac{20\theta}{Re_\theta^{\frac{1}{4}}}$	$0.9U_\infty$	Eq. (4.5)

Table 4.1. Location of planes, turbulent length scales and the associated convection velocities.

4.1.1. Near Wall region

A large consensus exists concerning turbulent structures in the buffer layer. Jeong et al. [47] obtained ensemble averages of the velocity fields surrounding the vertical structures. This data provides precise structural information about the eddies present in the buffer layer. Table 4.1 gives the location of the center, sizes and convection velocity of various turbulent structures in the various modes. The normal length scale of the near wall region is fixed by the lowest altitude of y_1^{low}. The transverse length scale is slightly larger.

4.1.2. Logarithmic layer and wake region

When it comes to structures populating the logarithmic region and the rest of the boundary layer, such an analysis is by far more difficult. In fact, a lot of different eddy models have been proposed in the past to account for the turbulent scales distribution, boundary layer intermittency and structural angles. From recent numerical and experimental evidence, fluid dynamicists agree that the logarithmic region is populated with hairpinlike vortices that are organized in packets and evolve across the boundary layer to increasingly larger scales. In recent numerical studies,

del Alamo et al. [48] managed to educe the coherent structures in the logarithmic layer. As a result, they demonstrate that this region is populated with intense self-similar vortex clusters. Their instantaneous form cannot be described visually, but their ensemble average corresponds to a hairpin-like structure. Moreover, the size of these clusters scales with their distance to the wall.

In the present method, the simple approach of introducing at the inlet the most representative structure of this layer—a hairpin—is adopted. A hairpin structure may be decomposed into two slanted legs connected by a transverse head. Legs are elongated and inclined in the streamwise-wall normal plane, whereas heads are more elongated in the transverse direction. Following these observations, sizes and aspect ratios are chosen and a mode $p=2$ is defined, representing either the legs or the head of a hairpin.

The analytical expressions of the shape functions are defined below.

$$f_{l_x,1,p=1,2}(\tilde{x})f_{l_y,1,p=1,2}(\tilde{y})f_{l_z,1,p=1,2}(\tilde{z}) = G(\tilde{x})G(\tilde{y})H(\tilde{z}) \tag{4.9}$$

$$f_{l_x,2,p=1,2}(\tilde{x})f_{l_y,2,p=1,2}(\tilde{y})f_{l_z,2,p=1,2}(\tilde{z}) = -G(\tilde{x})G(\tilde{y})H(\tilde{z}) \tag{4.10}$$

$$f_{l_x,3,p=1,2}(\tilde{x})f_{l_y,3,p=1,2}(\tilde{y})f_{l_z,3,p=1,2}(\tilde{z}) = G(\tilde{x})H(\tilde{y})G(\tilde{z}) \tag{4.11}$$

where,

$$H(\tilde{\zeta}) = \frac{1 - \cos(2\pi\tilde{\zeta})}{2\pi.0.44\sqrt{l_\zeta}} \tag{4.12}$$

and G is a Gaussian-type distribution function

$$G(\tilde{\zeta}) = \frac{2}{\sqrt{l_\zeta\pi}}exp\left(-\left(2\tilde{\zeta}\right)^2\right) \tag{4.13}$$

with $\tilde{\zeta} = \tilde{x}, \tilde{y}, \tilde{z}$.

Finally, the rest of the boundary layer is filled with Gaussian isotropic structures, for which aspect ratios are all unity and shape functions are defined as shown in Table 4.1. For this mode, no particular shape is imposed. Consequently, a random sign is given to each component so as to meet the zero covariance condition, as already mentioned above. Furthermore, two modes $p = 3$ and $p = 4$ are introduced in the outer scaling region in order to account for the growth of scales

in the outer region. In accordance with the work of Quadrio and Luchini [49] and Adrian et al. [50], their convection velocity is set equal to $0.8U_\infty$. The mode shape is given by,

$$f_{l_x,j,p=3}(\tilde{x})f_{l_y,j,p=3}(\tilde{y})f_{l_z,j,p=3}(\tilde{z}) = G(\tilde{x})G(\tilde{y})G(\tilde{z}) \tag{4.14}$$

where $j = 1, 2, 3$ describes the velocity component in the streamwise, wall-normal and spanwise directions respectively.

The function $H(\tilde{\zeta})$ determines the arrangement of the vortices, while the function $G(\tilde{\zeta})$ defines the spatial distribution of the vortices.

The length scales in the inflow planes $p = 2, 3$ were decided on using results of two-point correlations of turbulent boundary layers at several Reynolds and Mach numbers. The main dependence on Re_θ has been determined.

In the defect-law region i.e. the logarithmic region and the beginning of the wake region, the length scales in the streamwsie, the wall-normal, and the spanwise directions are determined by a scaling relation based on the momentum thickness and the Reynolds number Re_θ that is adapted from the Blasius skin-friction formulation,

$$l_{x,p=2} = \frac{36\theta}{Re_\theta^{\frac{1}{4}}} \, , \tag{4.15}$$

$$l_{y,p=2} = \frac{12\theta}{Re_\theta^{\frac{1}{4}}} \, , \tag{4.16}$$

$$l_{z,p=2} = \frac{15\theta}{Re_\theta^{\frac{1}{4}}} \, . \tag{4.17}$$

The eddies are stretched in the streamwise and the spanwise direction in the second plane $p = 2$ of the NLDE inflow boundary and their length scales scale with the Reynolds number Re_θ. In the outer layer i.e. $p = 3$, the length scales are calculated by

$$l_{x,p=3} = \frac{50\theta}{Re_\theta^{\frac{1}{4}}} \quad , \tag{4.18}$$

$$l_{y,p=3} = \frac{20\theta}{Re_\theta^{\frac{1}{4}}} \, , \tag{4.19}$$

$$l_{z,p=3} = \frac{20\theta}{Re_\theta^{\frac{1}{4}}} \quad . \tag{4.20}$$

In this plane, the eddies are stretched only in the streamwise direction.

It should be emphasized that the presented method only requires the velocity and turbulent viscosity distribution at the inlet to generate the synthetic structures. Furthermore, unlike the approach of Jarrin et al. [43], which requires a controlled forcing for an efficient RANS-to-LES transition, no control planes downstream of the inlet are necessary such that the computational complexity is reduced. It is more or less straightforward to combine the synthetic inflow formulation with any RANS turbulence model in a zonal RANS–LES method. Furthermore, for compressible boundary layer flows, Morkovin's hypothesis (Smits and Dussauge, [51]) is applied at the LES inflow boundary to relate the density fluctuations via the assumption of locally constant pressure and velocity fluctuations and to enforce the strong Reynolds analogy (SRA) (Smits and Dussauge, [51]).

4.2. Verification of the Synthetic Eddy Method

The modified synthetic eddy method described above has been tested in the following steps.

1. Isotropic turbulence with $u_{rms} = 1$ m/s was used as an input. The normal stresses of the prescribed Reynolds stress tensor were set to unity and the other components were set to zero.
2. Prescribed stress tensor profiles based on experimental results obtained for zero pressure gradient flat plate boundary layers were used as input and the subsequent stress tensor from the SEM was compared to the input.

4.2.1. Isotropic turbulence case

Time averaged statistics extracted from the simulation were compared with the desired results (the input Reynolds stress tensor).

Isotropic synthetic fluctuations were generated on a two-dimensional plane with the modified SEM. A uniform mean flow of $U_o = 10$ m/s in the x-direction normal to the inlet plane and rms velocity of $u'_o = 1$ m/s were used. In wind-tunnel experiments, this situation is created by passing a uniform stream through a grid.

Shown below in Figures 4.2 and 4.3 are the time histories of the time averaged one point $< u' >, < v' >$ averages and second order correlations $< u'u' >$ and $< u'v' >$. The two graphs are shown for a point in each of the two planes having different shape functions. An input rms velocity of 1 m/s should correspond with the $< u'u' >$ component going to 1 m/s while the other time averaged shear stresses and instantaneous velocities should go to zero because they are uncorrelated and independent of each other.

Figure 4.4 is the normal stress component $< u'u' >$ extracted at the end of the calculation and depicted for all the wall-normal points at a particular spanwise location.
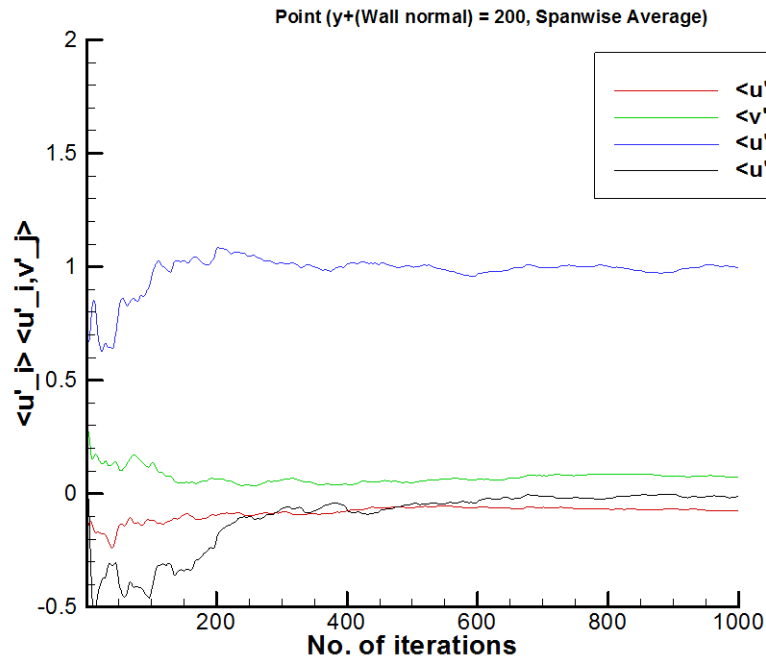
Figure 4.2: Time history of $< u' >, < v' >$ and second order correlations $< u'u' >$ and $< u'v' >$ at $y^+ = 200$.
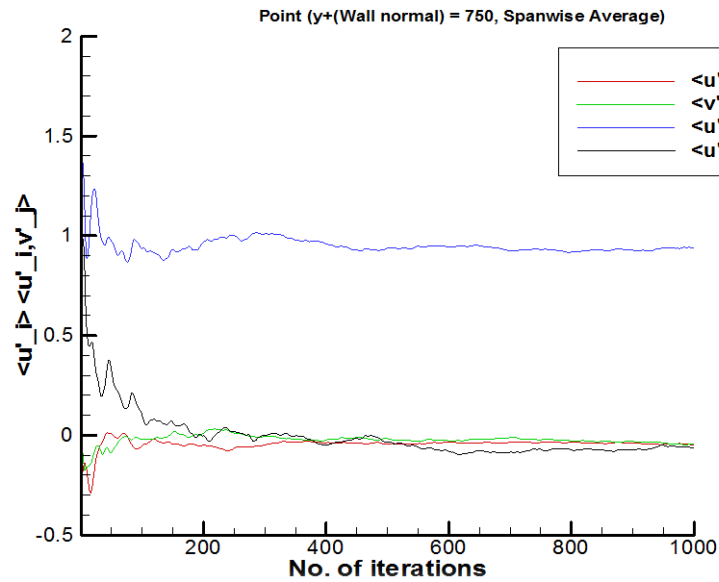
Figure 4.3: Time history of $< u' >, < v' >$ and second order correlations $< u'u' >$ and $< u'v' >$ at $y^+ = 750$.

Figure 4.4: Time averaged u_{rms} averaged for all points in the wall normal direction, extracted at $t = 1000$ time steps.

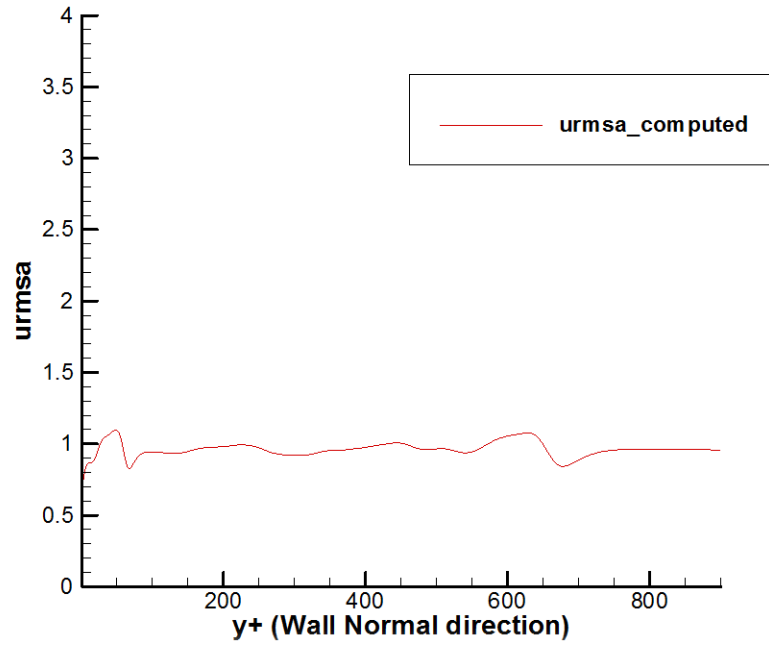### 4.2.2. Prescribed stress tensor testing

Prescribed stress tensor profiles extracted from experimental results for a zero-pressure-gradient flat-plate boundary layer were used as input to the simulation. The output was then compared to the prescribed profiles. The results are shown in Figures 4.5 and 4.6 below.

Figures 4.5 and 4.6 show the prescribed stress tensor and their comparison with the stresses obtained from the SEM. A comparison of these figures shows that there is a good match between desired and simulated values.
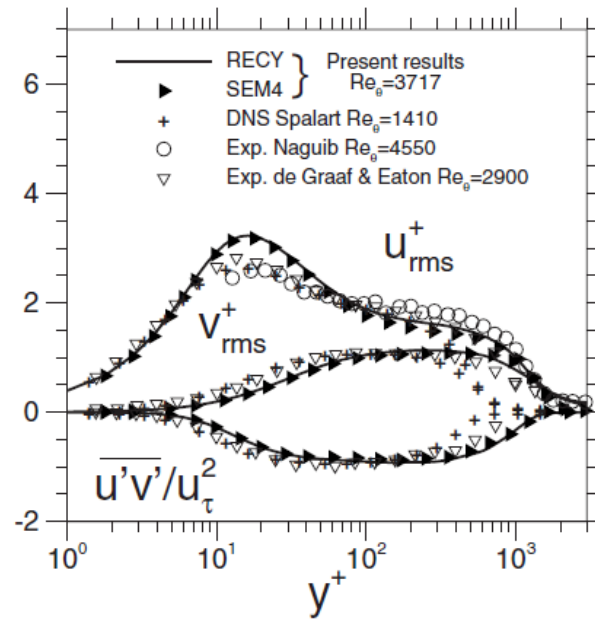
Figure 4.5: Curves representing various components of the input Reynolds stress tensor [45]
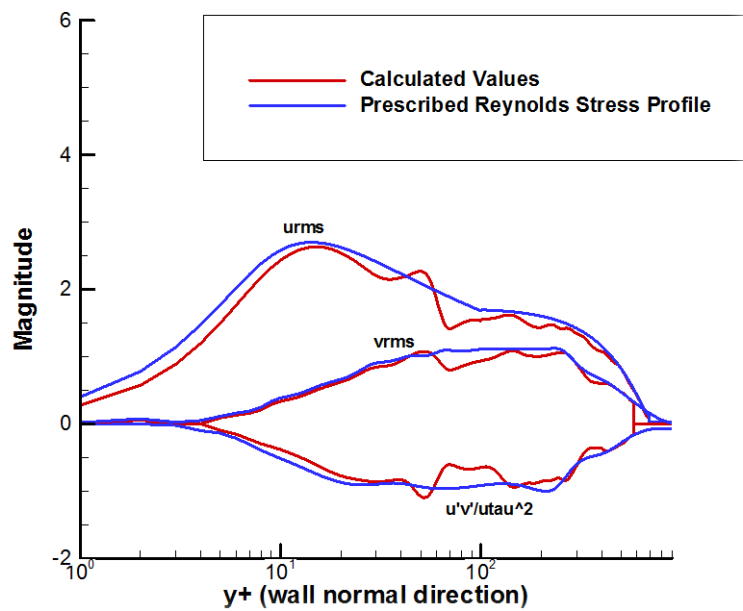

Figure 4.6: Graph showing comparison of input Reynolds stress compared to stresses obtained from the SEM simulation
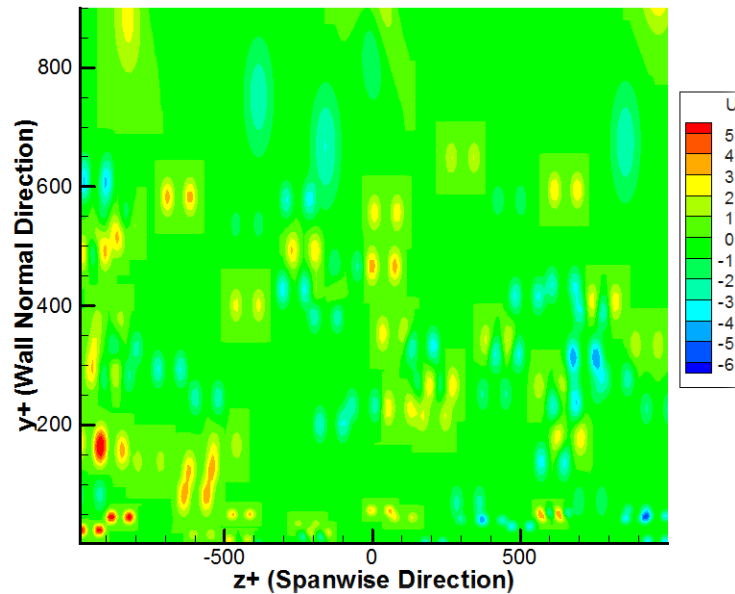
Figure 4.7: u' fluctuations generated at the inlet plane using the modified SEM method

Figure 4.7 is a representation of the inlet plane of the standalone code and how the turbulent spots look in at the plane. The difference in eddy shapes is clearly visible in the regions where the different modes are described.

4.3. Noise Calculations

The next chapter describes the cases set up for the testing of the NLDE concept for trailing edge noise predictions. Two cases have been considered: a Flat Plate Zero Pressure Gradient trailing edge and a NACA 0012 airfoil trailing edge.

Chapter 5

Noise Prediction

Two cases have been set up to validate the NLDE model and the CHOPA code with the Synthetic Eddy Method (SEM) for the trailing edge noise prediction. The CHOPA code has already been tested for a variety of cases for jet noise predictions. Also standard test cases like Gaussian Pulse propagation and interpolation on finer grids have been performed to validate CHOPA. The SEM code has also been tested independently as mentioned in the previous chapter. It has been integrated into the CHOPA code as an additional boundary condition for turbulence injection. The flat plate and the NACA 0012 airfoil have been used to obtain noise predictions using a URANS base flow and then using a fine LES grid in the NLDE domain to obtain appropriate values.

5.1. Flat Plate Trailing Edge.

A zero pressure gradient flat plate boundary layer is used as a first validation case for testing CHOPA capabilities with SEM for turbulence injection. To set up the case, a coarse grid is constructed for the base flow calculation using the Spalart-Allmaras (SA) model and the Unsteady Reynolds Navier Stokes (URANS) settings in CHOPA. The grid used for the URANS case is made up of a hyperbolic tangential stretching function in the wall-normal (y) direction to resolve the boundary layer development and is also clustered near the leading edge to resolve the turbulent boundary layer.

The grid used to obtain the URANS base flow calculations is a two-block structure consisting of 329 points in the streamwise (x) direction, 209 grids in the wall-normal (y) direction and 5 points in the spanwise (z) direction for each block. The URANS formulation in CHOPA requires at least 4 points in the spanwise (z) direction for the application of the spatial stencil. A quasi-two

dimensional simulation is performed. The leading edge starts at $x = 0.0$ m and the flat plate extends to 0.74m where it is cutoff, giving the trailing edge. The mean density has been set to 1.2 kg/m^3 and pressure to 99.35 kPa. The domain is operating at Re $\approx 1.849 \times 10^7$ and the free stream Mach number (M) is $= 0.09991$. The values specified above were chosen to correspond to the conditions specified in Pamies et al.[6] and a specific case of Roidl et al.[7] Also, the values for the Reynolds stress tensor for these cases is readily available. The thickness of the boundary layer has been verified by checking against available data. The boundary conditions for the RANS solution are subsonic inflow at the inlet, an adiabatic viscous wall at the lower boundary on the plate, Riemann boundary conditions on the upper boundary and the outlet, and periodic boundary conditions in the spanwise direction. The no-slip condition starts at the leading edge and extends to $x = 0.74$ m at the trailing edge. After this a connector boundary condition is applied to join the two blocks and simulate the free wake
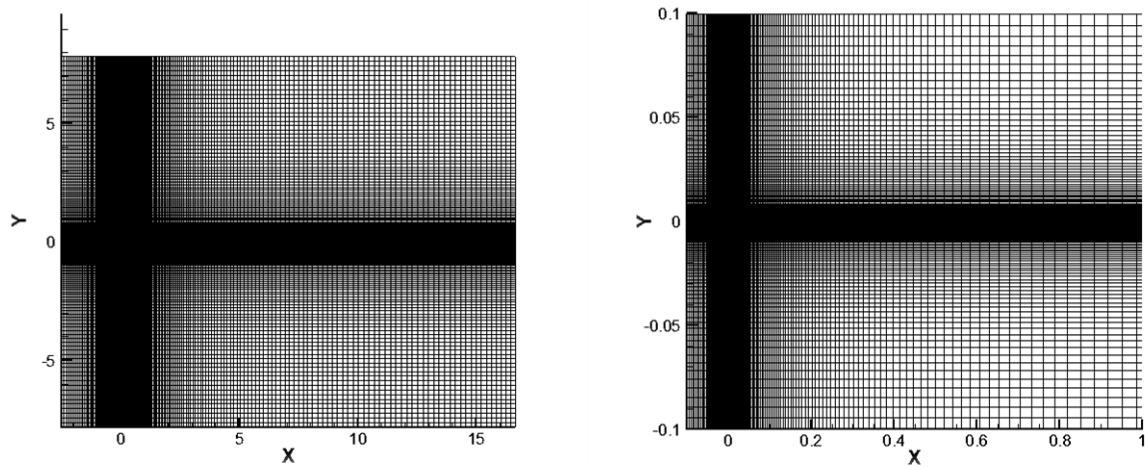
Figure 5.1: Trailing Edge Flat Plate coarse grid constructed for URANS base-flow calculation.

Figure 5.1 is a depiction of the coarse grid used in the URANS case. The left figure shows the whole domain with the appropriate clustering visible near the leading edge and the flat plate. The right figure is a zoomed in version of the grid near the flat plate region. The leading edge is far enough from the domain inlet that it is not affected by the conditions there. The turbulent boundary layer is free to evolve without influence from the domain boundaries.

The URANS solution is run until the flow is statistically steady. An accurate RANS mean flow solution is important for running the NLDE simulation. The disturbances are solved around the mean equation and require accurate τ_{wall} and boundary layer thickness δ_0. Also these values need to be considered when choosing inputs for the SEM inflow boundary condition. Figure 5.2 shows the URANS solution with the streamwise velocity profile. The trailing edge has been indicated at $x = 0.74$ m and contours of the streamwise velocity of the domain are shown, which is magnified near the trailing edge. This is to show that the values that are used in the NLDE fine grid domain are accurate and serve as the proper base flow solution for this case.
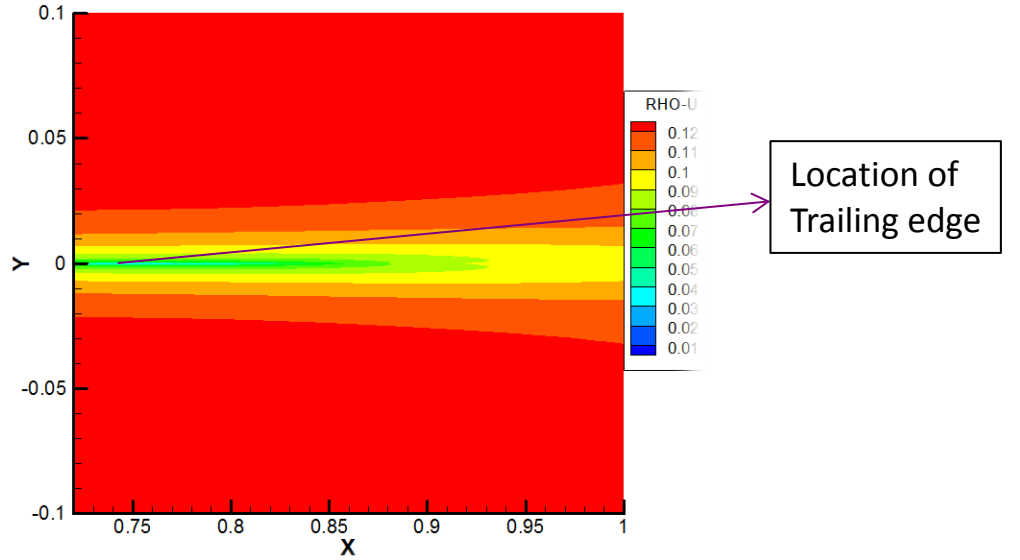

Figure 5.2: Trailing edge RANS results (velocity is nondimensionalized using speed of sound, i.e., $v = v/a^*$, with $a^* = 340\ m/s$).

Once the URANS base flow was obtained the NLDE grid was constructed. The NLDE fine grid starts at a downstream location of 0.7205 m which corresponds to a Reynolds number based on momentum thickness, $Re_\theta = 3551$. It consists of two blocks for the upper and lower part of the flat plate, joined by a connector boundary condition downstream of the trailing edge for the part shared by the blocks. The input friction velocity is $u_\tau = 1.126$ m/s and the inlet boundary layer thickness $\delta_0 = 0.0162$ m. The grid has the following dimensions for each block: $L_x = 17\delta_0$, $L_y = 1.7\delta_0$, and $L_z = 1.7\ \delta_0$, with $460 \times 88 \times 133$ grid points in the x (streamwise), y(wall normal) and z(spanwise) directions, respectively. The grid spacing is such that a grid resolution

of $\Delta x^+ < 20$, $\Delta y^+ < 1$, and $\Delta z^+ < 12$ is maintained throughout. This is done to ensure that the large eddies that are to be simulated are resolved at all times. The trailing edge starts at a downstream location of $x = 0.739$. The base flow solution is interpolated onto the grid. The above parameters have been chosen so that the results can be verified with the Pamies [45] and Roidl [46] cases that use the same input data.
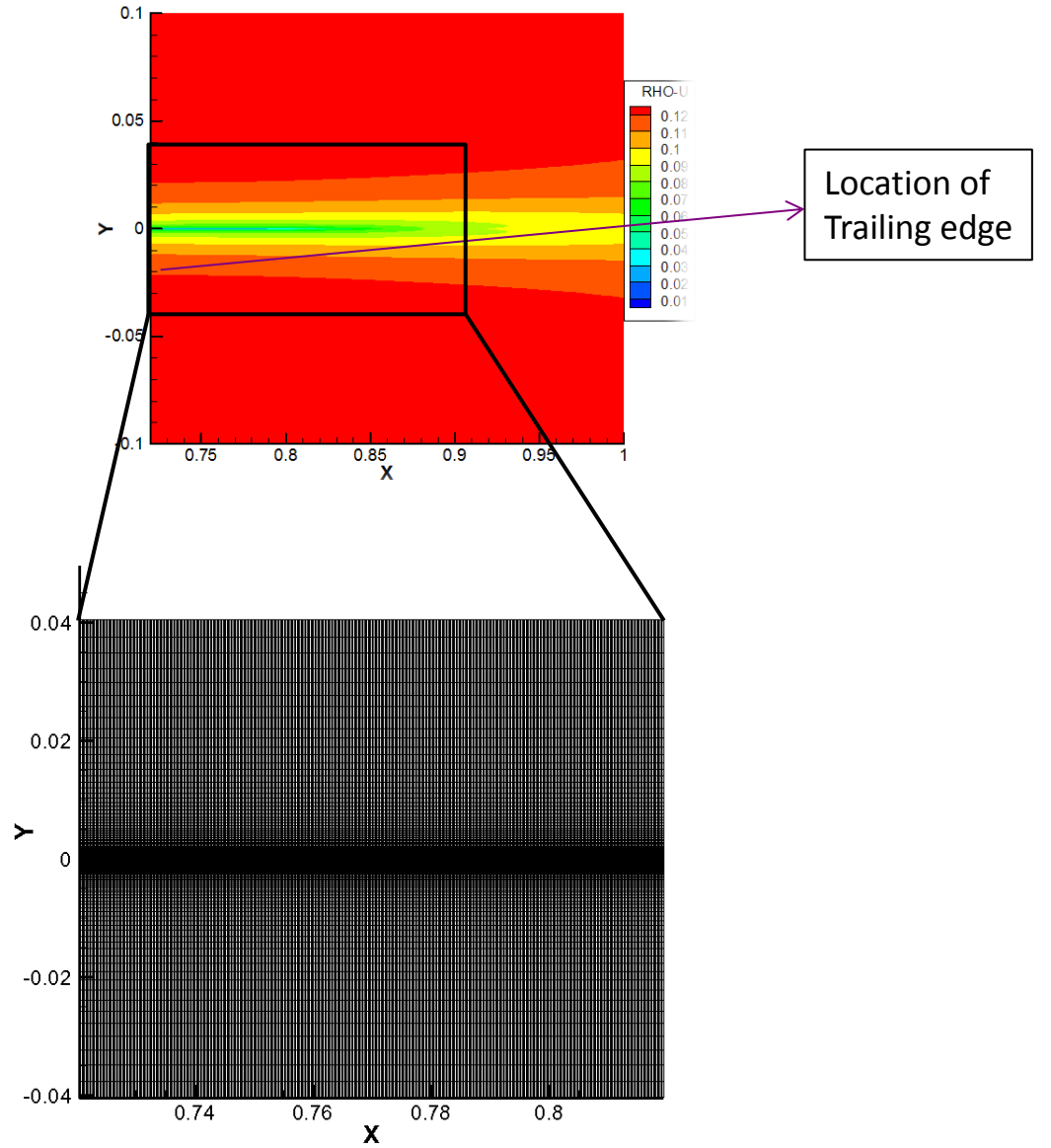
Figure 5.3: 2-D section of the Cartesian grid used in the NLDE domain. The NLDE domain has been restricted to the region shown above.

Figure 5.4 shows contours of the streamwise velocity of the RANS solution interpolated onto the NLDE grid. The URANS base flow interpolation on the NLDE fine grid domain has been verified and depicted in figure 5.5. The velocity profile has been taken at two downstream locations to check if the interpolation is accurate.
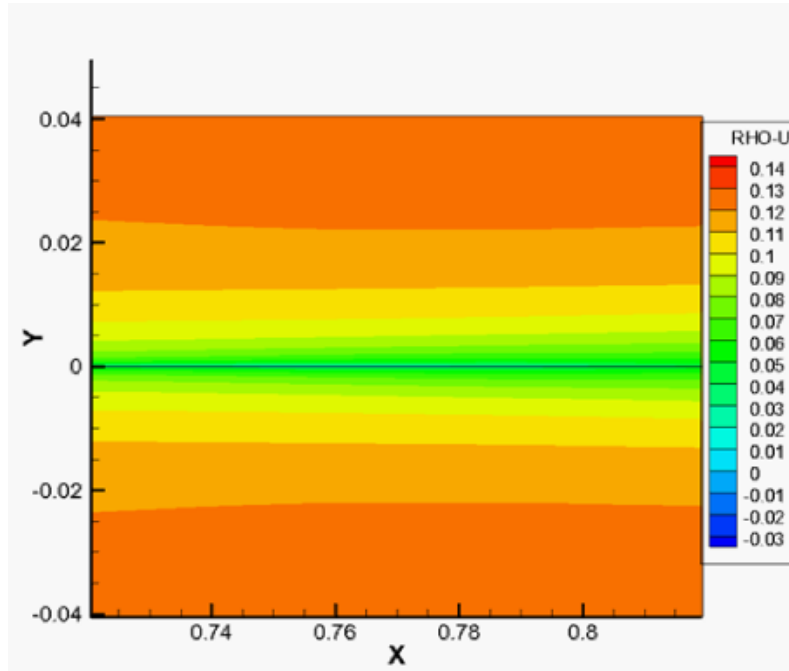
Figure 5.4: RANS solution interpolated onto the NLDE grid.
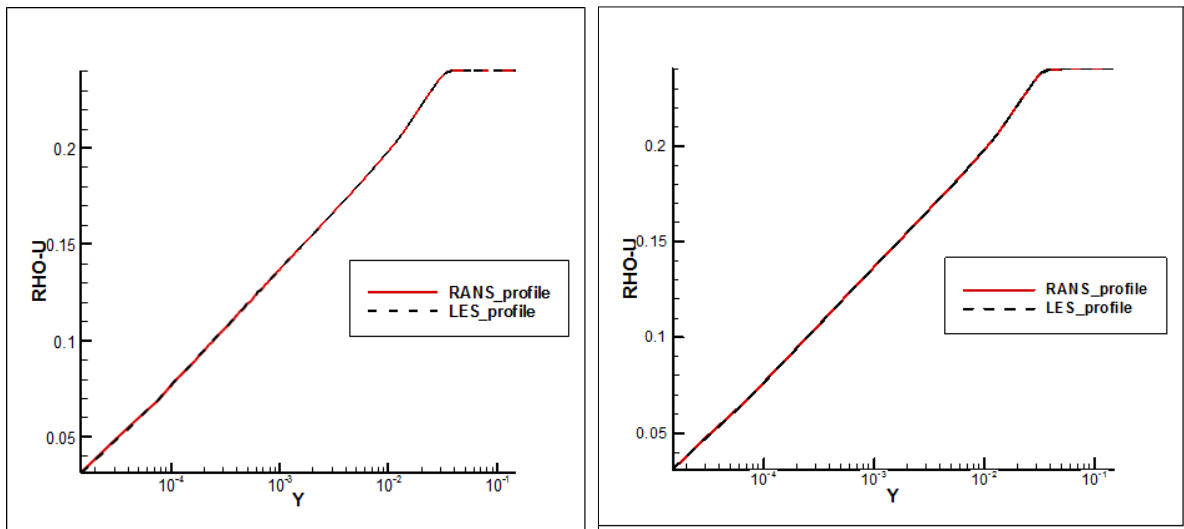
Figure 5.5: u (streamwise) velocity profile at $x = 0.73$ m and $x = 0.74$ m

The Synthetic Eddy Method (SEM) has been used to initiate the turbulence for the NLDE domain. Permeable acoustic data surfaces (ADS) are used to extract the momentum, density and pressure fluctuations generated by the interaction of the eddies with the trailing edge. Figure 5.6 shows a representation of the multi-block grid used and the FW-H (Ffowcs Williams--Hawkings patches (ADS) associated with them.
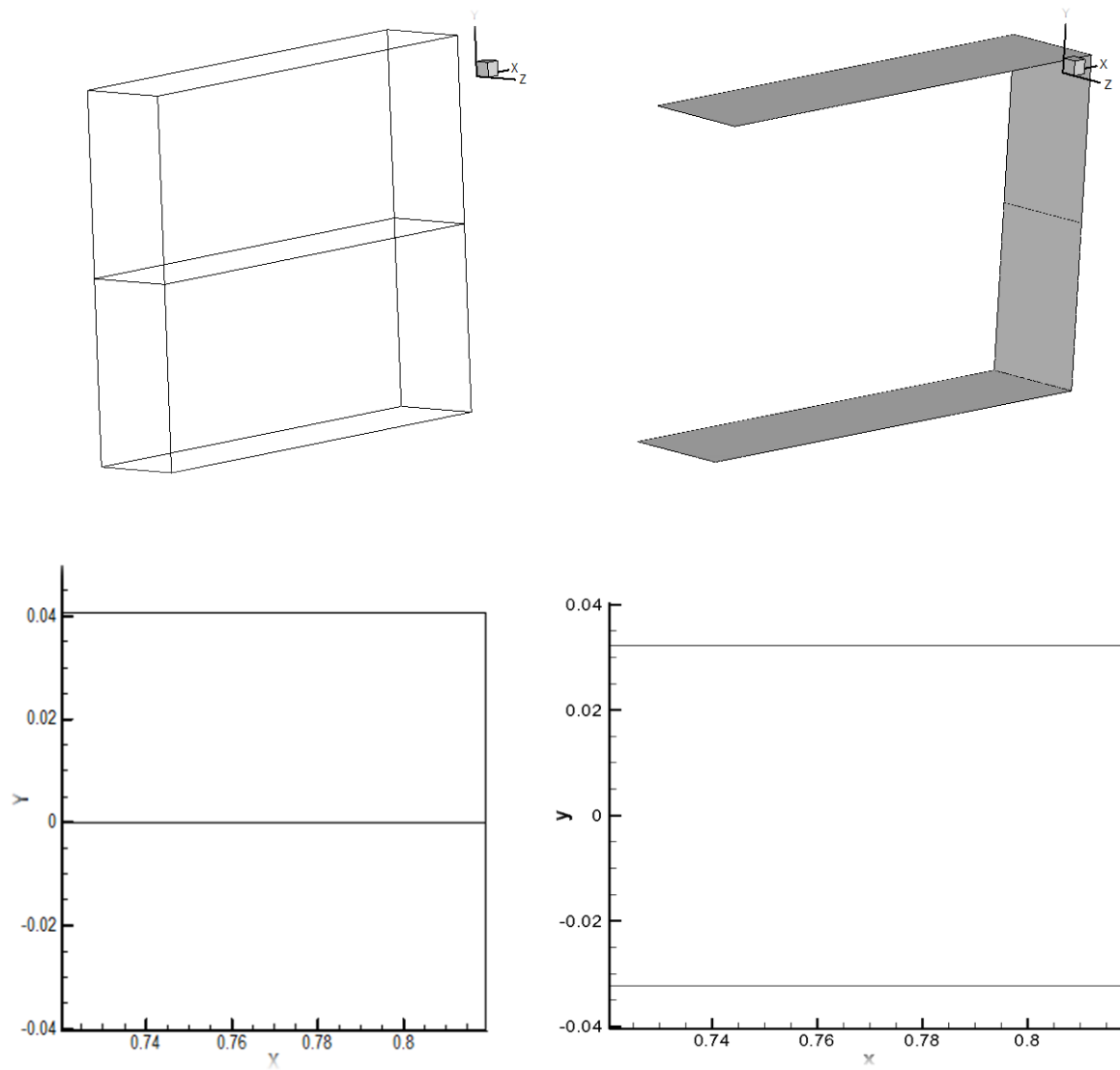
Figure 5.6: 3-D representation of the Cartesian grid boundaries (top-left), 3-D representation of the FW-H patches (top-right), 2-D representation of the Cartesian grid boundaries(bottom-left),2-D representation of the FW-H patches (bottom-right)

CHOPA flow solutions at the selected FW-H patches are obtained as described in the CHOPA manual [27]. These need to be converted to match the functional data file format for PSU-WOPWOP for the relevant loading data (ρ, ρu, ρu, ρu and $p - p_0$ (gage pressure)). A converter has been developed to read in the binary flow solution file output from CHOPA and apply the appropriate headers describing input flags needed in PSU-WOPWOP.

Changes in the momentum variables are also need to be made to match with the assumptions on which the permeable surface version of Farassat's formulation 1A is based. These are carried out using the base and ambient flow velocities present in the domain. The assumption in PSU-WOPWOP is that the fluid medium is stationary and the airfoil or ADS is moving through the medium. This is in contrast to the flow solutions out of CHOPA where the airfoil is assumed to be stationary and the fluid flows over it. The momentum fluctuations are scaled to dimensional values and free stream velocity is added to the fluctuations on the ADS to match the requirements for PSU-WOPWOP.

The solutions once converted to PSU-WOPWOP input files (patch and loading data files) are then used for the prediction of noise. PSU-WOPWOP case files were generated for the permeable surface method and Figure 5.7 depicts the observer configuration around the FW-H surfaces. 360 observers are used for the far-field noise at a distance of 1m. The noise results are described below. The OASPL sound pressure level is described in Figure 5.8. ADS data from only the two patches (top and bottom) are considered as the downstream patches contaminate the solution by dominating the fluctuation velocities. The lobe shapes do not match experimental and LES data. This may be a fact of there being not enough time-histories to get a full account of the broadband spectrum required to capture all frequencies. Acoustic pressure data was also gathered for a single observer placed directly over the trailing edge at a distance of one meter. Figure 5.9 shows the acoustic pressure data collected using flow data on all ADS. The data seems to be generating an acoustic signal but hasn't reached a mean value. Also, acoustic spectrum data was collected for the same observer, shown in Figure 5.10.

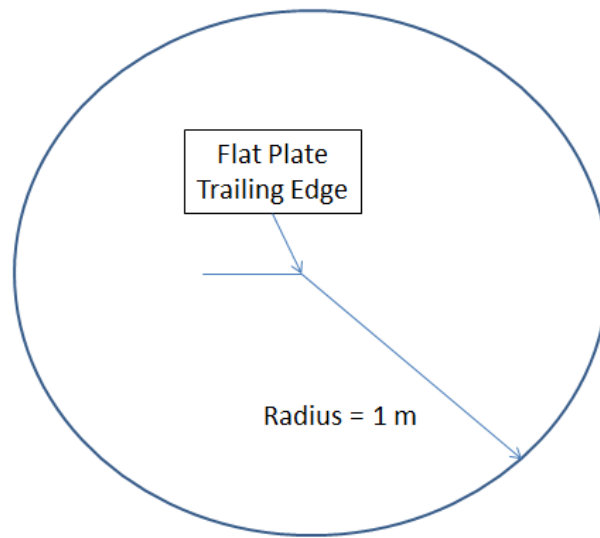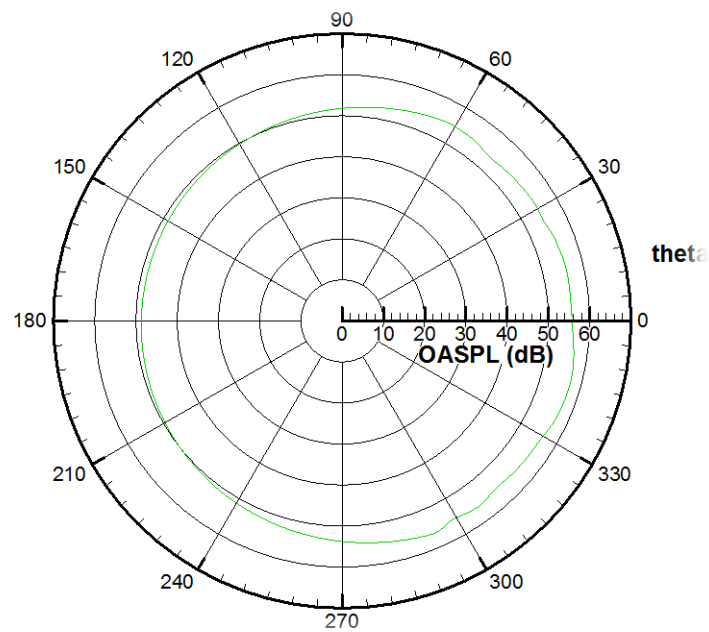Figure 5.7: Observer configuration for the Flat Plate Trailing Edge Noise prediction.

Figure 5.8: OASPL predictions for the Flat Plate Trailing Edge Noise.
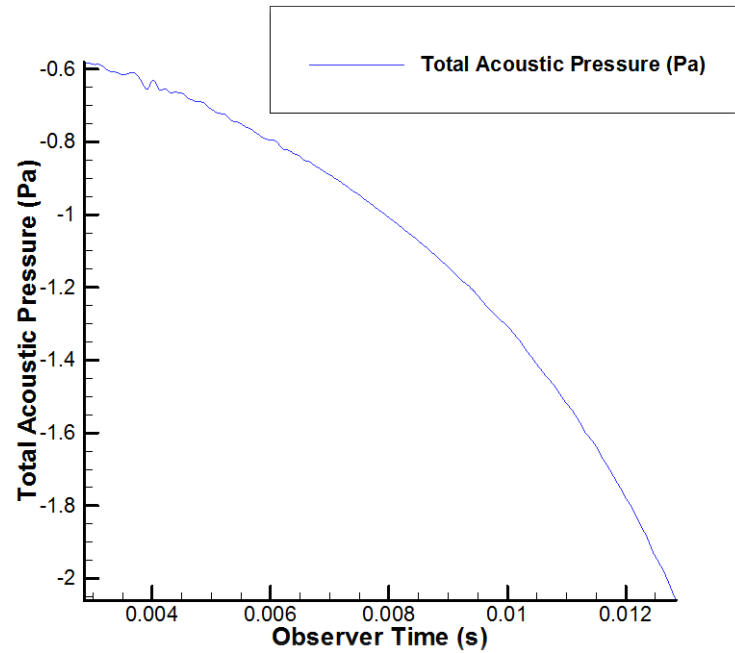
Figure 5.9: Acoustic pressure (Pa) at an observer directly above the trailing edge at a distance of 1 m from the trailing edge
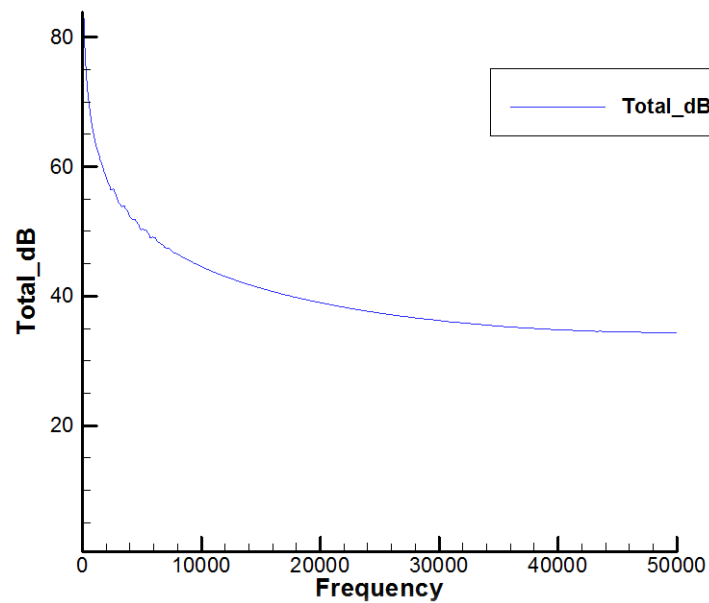

Figure 5.10: Sound Pressure Level (SPL) spectrum for an observer directly above the trailing edge at a distance of 1 m from the trailing edge

5.2. NACA 0012 Trailing Edge Case

The NACA 0012 airfoil is selected to obtain airfoil trailing edge noise results. This airfoil was commonly used in helicopter rotor blades in the past. Also, there is extensive literature available for the NACA 0012 airfoil and the results can be compared to noise results from the various studies that have been performed. The procedure to set-up the NACA 0012 trailing edge simulation is the same as the one described for the flat plate trailing edge case. The airfoil is set at zero degrees angle of attack for all the simulations used in the thesis.

The first part of the case setup is the creation of the RANS coarse grid for the base flow URANS simulation. The grid used is obtained from the turbulence archive test cases from the NASA turbulence resource[52]. The topology is a so-called "C-grid," with the grid wrapping around the airfoil from the downstream far-field, around the lower surface to the upper, then back to the downstream far-field again; the grid connects to itself in a one-to-one fashion in the wake. The grid used has 897 x 257 x 4 points in the *x, y* and *z* directions respectively. There are 513 x 4 points on the airfoil surface. The grid has been divided into two-blocks and initialized with the mean density set to 1.225 kg/m^3 and pressure to 101.33 kPa. The domain is operating at $Re_c \approx$ 2.407x10^6 based on the airfoil chord and the free stream Mach number $M = 0.09991$. The far-field boundary uses a Riemann boundary condition while the airfoil surface uses the adiabatic solid wall to simulate the solid surfaces. This grid has also been verified by simulating the NACA 0012 airfoil at 0 degree angle of attack and M=0.15. These values are used to verify results available as the validation case on the NASA turbulence resource. The boundary layer profile is tested against the law of the wall (LOTW), as shown in Figure 5.11 The skin-friction (C_f) and pressure (C_p) coefficients have also been tested for the Mach number mentioned aboveFigure 5.12 shows the friction and pressure coefficients superimposed on the graphs available on the website. Good agreement is observed between all values obtained from CHOPA compared to experimental and CFD code solutions available on the NASA turbulence website.
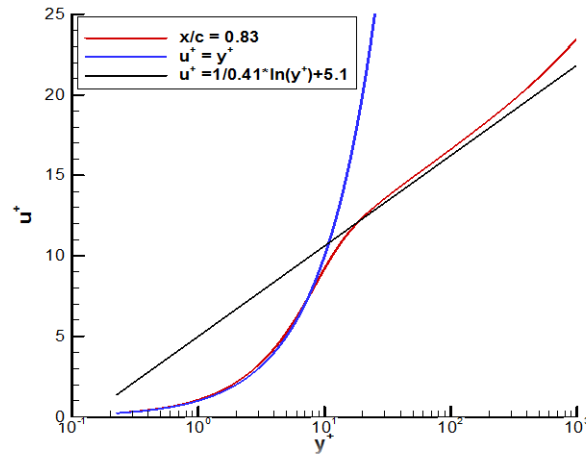
Figure 5.11: Boundary layer profile obtained from the RANS SA simulation from CHOPA(red line) superimposed on the Law of the Wall plot.
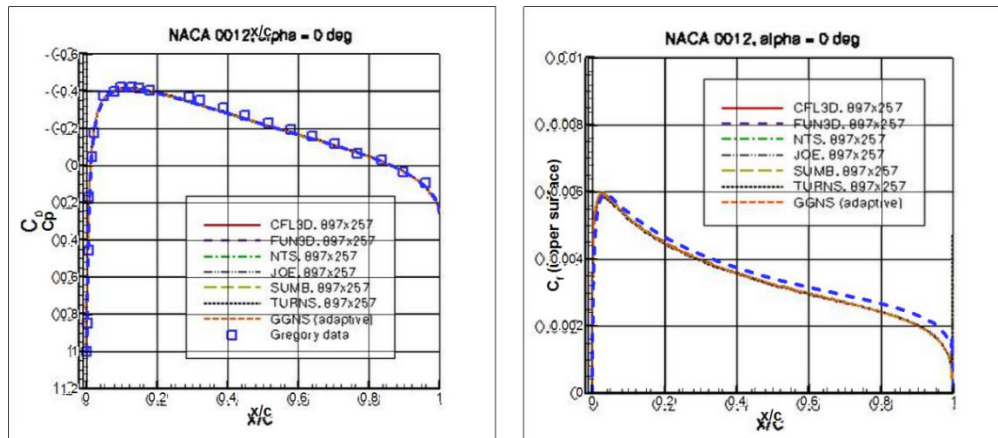
Figure 5.12: C_f (left) and C_p (right) comparison with data from various solvers. The dashed blue line indicates values obtained from CHOPA.

The NLDE grid is constructed in a limited domain near the trailing edge. The grid starts at a streamwise location of $x = 0.7$ m and extends up to $x = 1.4$ m to resolve some part of the wake. The wall-normal extent of the grid is 0.1 m above the airfoil surface at the inflow. The spanwise length is 0.0405 m. Grid spacing in the wall-normal and spanwise directions has been maintained to resolve eddies that are injected using the SEM. $y^+ \approx 0.2$ at the first point over the airfoil surface in the wall normal direction. $\Delta z^+ < 12$ is used in the spanwise direction to get the appropriate 3-D effects of the turbulence. $\Delta x^+ < 100$ is maintained in the streamwise direction

and is a value used commonly in many LES simulations of the NACA 0012 airfoil. The total grid points are 500 x 117 x 133 in one block. Two blocks are used, one each for the pressure and suction side of the airfoil. Also permeable acoustic data surfaces are used to resolve the acoustic data required as input to PSU-WOPWOP. Figure 5.13 (right) shows the ADS for the NLDE NACA 0012 zero degrees angle of attack (AOA) case.
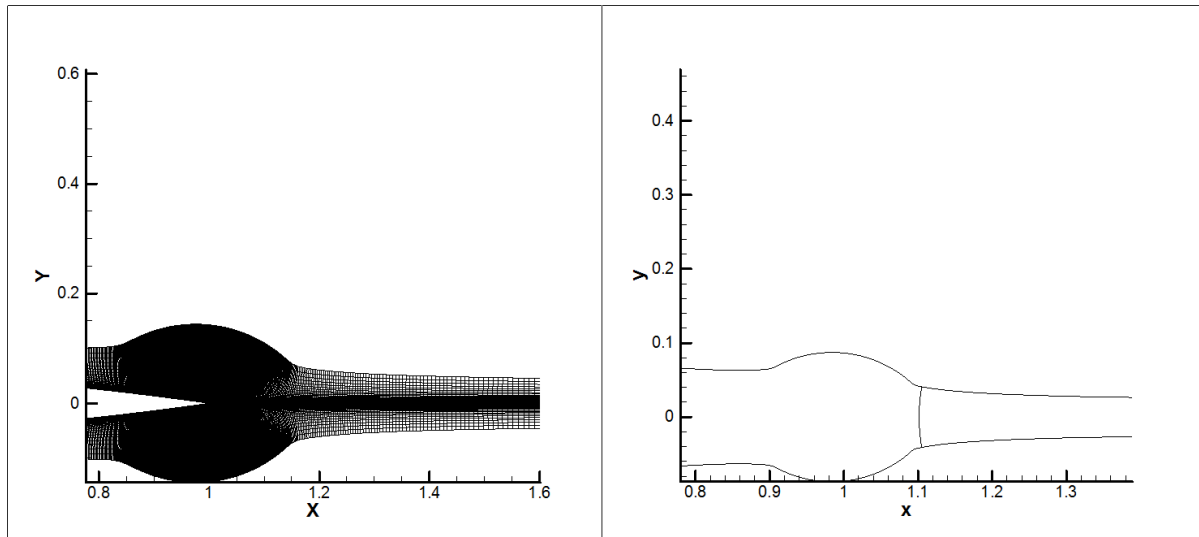
Figure 5.13: 2-D representation of Cartesian Grid boundaries and the FW-H surface (right)

Noise results were collected for a ring of observers at a distance (radius) of 5 m (5 chord lengths) from the trailing edge. 360 observers are used in the observer grid to resolve noise values at every 1 degree angle resolution. This is shown in Figure 5.14. Figure 5.15 shows the Overall Sound Pressure level directivity plots that should depict the dipole like character of the noise. The directivity plot shows little agreement with the dipole character. This may be due the fact that enough time history data of the unsteady fluctuations is not available to obtain the whole range of frequencies required for the broadband noise spectrum. A single observer was placed directly over the trailing edge at a distance of five meters above the trailing edge to gather the acoustic data pressure, shown in Figure 5.16. An acoustic signal seems to being generated. Spectrum data was also obtained for the same observer. This has been shown in Figure 5.17.
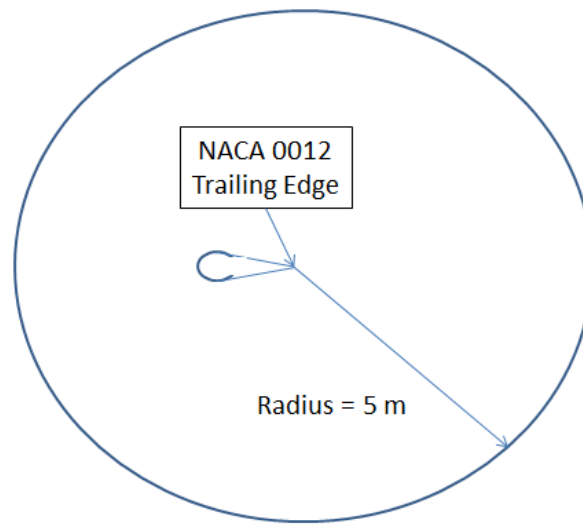
Figure 5.14: Observer grid around the NACA 0012 airfoil. 360 observers have been used at every 1 degree around the circle
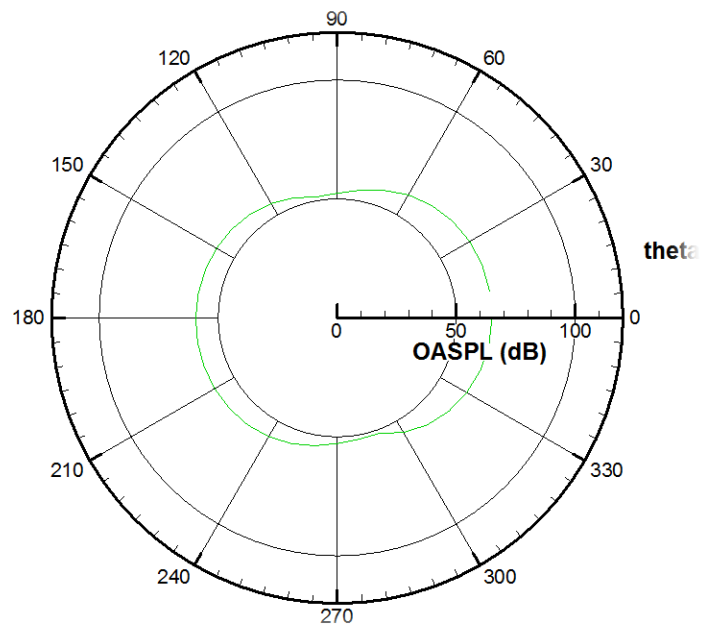
Figure 5.15: OASPL (dB) directivity for the NACA 0012 trailing edge
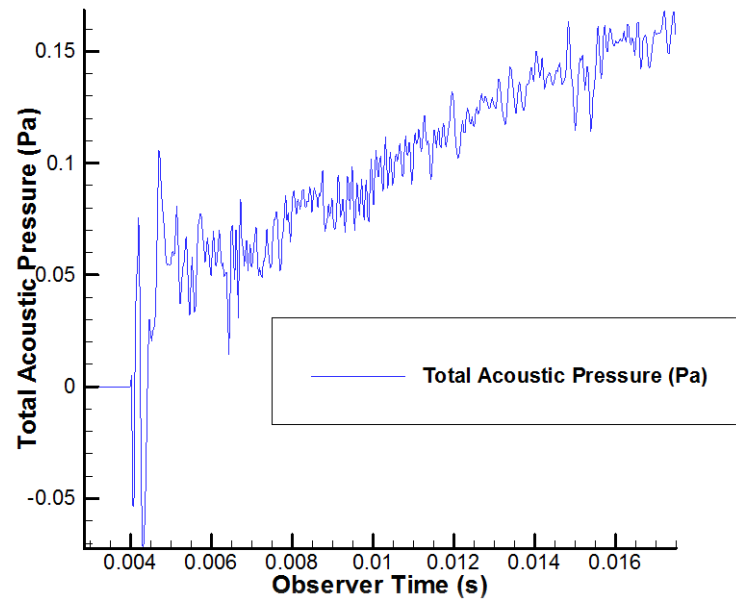
Figure 5.16: Acoustic pressure (Pa) at an observer directly above the trailing edge at a distance of 5 m from the trailing edge
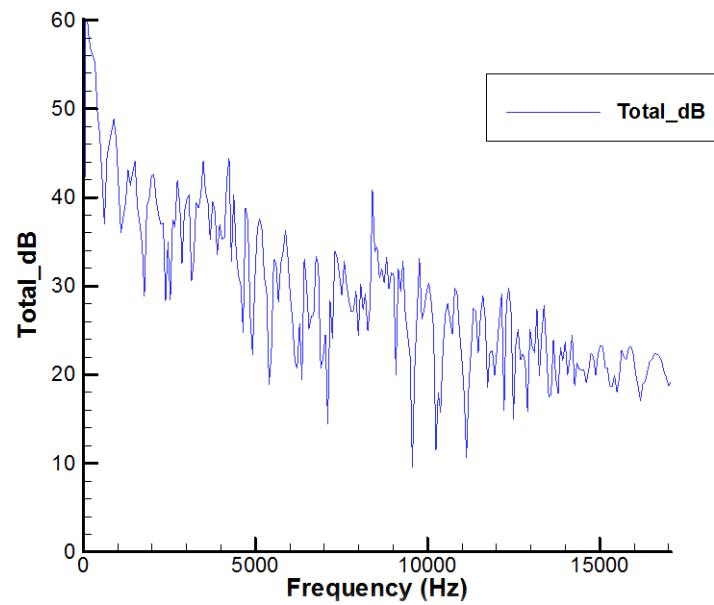
Figure 5.17: Sound Pressure Level (SPL) spectrum for an observer directly above the trailing edge at a distance of 5 m from the trailing edge

Chapter 6

Conclusions

This chapter summarizes the thesis and gives suggestions for future work and improvements that can be made to the CHOPA code.

6.1. Summary and Future Work

The CHOPA code has been validated for jet noise prediction and other simple cases like flow over a cylinder and Gaussian pulse propagation. The code has been used in this thesis for trailing edge noise prediction as a first principles approach to understand the underlying physics of the problem and to obtain a correct prediction of the TBL-TE noise generated by airfoil trailing edges. The hybrid RANS-NLDE formulation for tackling the problem leads to a computationally efficient solution using optimum techniques for the different parts of the problem. Turbulence injection in the form of the Synthetic Eddy Method has been integrated into CHOPA to enhance its capabilities and provide a means of adding physical turbulence to the NLDE domain. The NLDE domain is able to resolve unsteady flows and provide time histories of the acoustic pressure for noise prediction.

Preliminary noise results have been obtained for two representative test cases in CHOPA, namely the Flat Plate Trailing Edge and the NACA 0012 trailing edge. The RANS solutions for these are obtained using a standard SA model available in CHOPA itself. The code could be extended to use RANS results from any widely available solver to serve as a base flow for the NLDE domain.

6.2. Suggested Improvements

The CHOPA code with its extended SEM capabilities needs to be tested for additional cases. Also some improvements need to be made to the code to make it computationally efficient.

6.2.1. Additional Grid Refinement Studies

The NLDE grid currently used for the NACA 0012 is coarse in the stream-wise direction. Further studies need to be done with grids of different resolution to obtain an optimum grid level that balances eddy resolution with computational inexpensiveness.

6.2.2. Scalability for parallelization

The gathering of the unsteady momentum and pressure perturbation time histories on the Acoustic Data Surfaces takes a large amount of time for accurate noise predictions over the broad frequency range that TBL-TE exists over. Improvements in the parallelization routines can yield better results and would make the code capable of handling bigger grids and scaling over bigger computing clusters.

6.2.3. Testing with different airfoils

The current testing in CHOPA has been performed for a NACA 0012 airfoil at zero degree angle of attack. This is a symmetrical airfoil. To better approximate real world data, the NACA 0012 airfoil should be tested at different angles of attack and validate the noise characteristics obtained should be validated. Also some other representative airfoils should be tested which can extend CHOPA usage to the wind turbine industry where TBL-TE noise is also of significant concern.

6.2.4. Improvement in parallelization routines

The parallelization routines of CHOPA need to be improved to make it scalable for bigger domains. As the code develops, the 3-D accuracy should continue to be validated for full 3-D helicopter rotor simulations. Specific spanwise blade sections of interest can be simulated individually with CHOPA. These spanwise sections can be run simultaneously in PSU-WOPWOP for an overall estimate of the noise from the entire helicopter rotor.

Bibliography

[1]   Brooks, T. F., Pope, D. S., and Marcolini, M. A., "Airfoil self-noise and prediction," NASA RP 1218, 1989.

[2]   NWTC Information Portal (NAFNoise). https://nwtc.nrel.gov/NAFNoise. Last modified 24-September-2014

[3]   Doolan, C. J., Moreau, D. J., & Brooks, L. A. (2012). Wind turbine noise mechanisms and some concepts for its control. *Acoustics Australia*, 40(1), 7-13.

[4]   J.E. Ffowcs Williams, L.H. Hall. Aerodynamic sound generation by turbulent flow in the vicinity of a scattering half-plane. *Journal of Fluid Mechanics*, 40 (1970), pp. 657–670

[5]   M.J. Lighthill. On sound generated aerodynamically. I. General theory. *Proceedings of the Royal Society London A*, 211 (1952), pp. 564–587

[6]   M.S. Howe. A review of the theory of trailing edge noise. *Journal of Sound and Vibration*, 61 (1978), pp. 437–465

[7]   Brooks, T. F., & Hodgson, T. H. (1981). Trailing edge noise prediction from measured surface pressures. *Journal of Sound and Vibration*, 78(1), 69-117.

[8]   Parchen, R.. Progress Report DRAW, a Prediction Scheme for Trailing-Edge Noise Based on Detailed Boundary-Layer Characteristics. TNO Institute of Applied Physics TNO-report HAG-RPT-980023, 1998.

[9]   Boorsma, K. and Schepers, J. G., Enhanced Wind Turbine Noise Prediction Tool SILANT. *Proceedings of the 4th International Meeting on Wind Turbine Noise*, INCE-Europe, Rome, Italy, 2011.

[10]   Oerlemans, S. and Schepers, J. G., Prediction of Wind Turbine Noise and Validation Against Experiment. *International Journal of Aeroacoustics*, Vol. 8, 2009, pp. 555-584.

[11]   Kamruzzaman, M., Lutz, T., Herrig, A., and Kramer, E., Semi-Empirical Modeling of Turbulent Anisotropy for Airfoil Self Noise Predictions. AIAA Paper 2010-3878, 2010.

[12]   Amiet, R. K. "Noise due to turbulent flow past a trailing edge." *Journal of Sound and Vibration* 47, no. 3 (1976): 387-393.

[13]   Howe, M. S. "Trailing edge noise at low Mach numbers." *Journal of Sound and Vibration* 225, no. 2 (1999): 211-238.

[14]   W. Bechara, C. Bailly, P. Lafon, and S. Candel. Stochastic Approach to Noise Modeling for Free Turbulent Flows. *AIAA Journal* , 1994.

[15]   P.R. Spalart and S.R. Allmaras. A One-Equation Turbulence Model for Aerdynamic Flows. *AIAA Journal* , 1992.

[16]   Verhoeven, O. Trailing edge noise simulations. Diss. Master's thesis, Delft University of Technology, 2011.

[17]   Morris, P. J., Long, L. N., Bangalore, A., and Wang, Q., "A Parallel Three-Dimensional Computational Aeroacoustics Method Using Nonlinear Disturbance Equations," *Journal of Computational Physics*, Vol. 133, 1997, pp. 56–74.

[18]   Hu, F. Q., M. Y. Hussaini, and J. L. Manthey. Low-dissipation and low-dispersion Runge–Kutta schemes for computational acoustics. *Journal of Computational Physics* 124, no. 1 (1996): 177-191.

[19]   C. Tam and J. Webb. Dispersion-relation-preserving finite difference schemes for computational acoustics. *Journal of Computational Physics*, 107: 262-281, 1993.

[20]   Du, Y., "Supersonic jet noise prediction and noise source investigation for realistic baseline and chevron nozzles based on hybrid RANS/LES simulations," Ph.D. Dissertation, Dept. of Aerospace Engineering., The Pennsylvania State University, University Park, PA, 2011.

[21]   Brès, G. A., Brentner, K. S., Perez, G., and Jones, H. E., "Maneuvering Rotorcraft Noise Prediction," *Journal of Sound and Vibration*, Vol. 275 (3-5), 2003, pp. 719-738.

[22]   Brès, G. A., "Modeling of the noise of arbitrary maneuvering rotorcraft: analysis and implementation of the PSU-WOPWOP noise prediction code," MS thesis, Dept. of Aerospace Engineering, The Pennsylvania State University, University Park, PA, May 2002.

[23]   Perez G., "Investigation of the influence of maneuver on rotorcraft noise," MS thesis, Dept. of Aerospace Engineering, The Pennsylvania State University, University Park, PA, May 2002.

[24]   Christiansen, M., Brentner, K., & Morris, P. (2011). Trailing-Edge Noise Prediction Using the Non-Linear Disturbance Equations. In 17th AIAA/CEAS Aeroacoustics Conference (32nd AIAA Aeroacoustics Conference).

[25]   Jameson, Antony. "Time dependent calculations using multigrid, with applications to unsteady flows past airfoils and wings." AIAA paper 1596 (1991): 1991.

[26]   Jameson, Antony, and Timothy Baker. "Solution of the Euler equations for complex configurations." In 6th Computational Fluid Dynamics Conference Danvers, p. 1929. 1983.

[27]   Du, Y., User's Manual for CHOPA and the Companion Utilities, (2013)

[28]   Tam, Christopher KW, Jay C. Webb, and Zhong Dong. "A study of the short wave components in computational acoustics." *Journal of Computational Acoustics* 1, no. 01 (1993): 1-30.

[29]   Tam, Christopher KW, and Zhong Dong. "Radiation and outflow boundary conditions for direct computation of acoustic and flow disturbances in a nonuniform mean flow." Journal of Computational Acoustics 4, no. 02 (1996): 175-201

[30]   N. Li, E. Balaras, and U. Piomelli. Inflow conditions for large-eddy simulation of mixing layers. *Physics of Fluids*, 12(4):935–938, 2000.

[31]   W.K. George and L. Davidson. Role of initial conditions in establishing asymptotic flow behavior. *AIAA Journal*, 42(3):438–446, 2004.

[32]   Spalart, P. R., Direct Numerical Simulation of a Turbulent Boundary Layer Up to Re$_\theta$= 1410. *Journal of Fluid Mechanics*, Vol. 187, Feb. 1988, pp. 61–98.

[33]   Lund, T. S., Wu, X., and Squires, K. D., Generation of Turbulent Inflow Data for Spatially-Developing Boundary Layer Simulations. *Journal of Computational Physics*, Vol. 140, No. 2, Mar. 1998, pp. 233–258.

[34]   Urbin, Gerald, and Doyle Knight. Large-eddy simulation of a supersonic boundary layer using an unstructured grid. *AIAA Journal* 39, no. 7 (2001): 1288-1295.

[35]   K. Mahesh, P. Moin, and S. K. Lele, "The influence of entropy fluctuations on the interaction of turbulence with a shock wave," Thermosciences Division, Department of Mechanical Engineering, Stanford University Report No. TF-69, 1996.

[36]   Y. Na and P. Moin, "Direct numerical simulation of a separated turbulent boundary layer," *Journal of Fluid Mechanics*. 374, 379 (1998)

[37]   R. Kraichnan, "Diffusion by a random velocity field," *Physics of Fluids* 13, 22 (1970)

[38]   A. Smirnov, S. Shi, and I. Celik, "Random flow generation technique for Large Eddy Simulations and particle-dynamics modeling," *ASME Journal of Fluids Engineering* 123, 359 (2001)

[39]   P. Batten, U. Goldberg, and S. Chakravarthy, "Interfacing statistical turbulence closures with large-eddy simulation," *AIAA Journal* 42, 485 (2004)

[40]   N. D. Sandham, Y. F. Yao, and A. A. Lawal, "Large-eddy simulation of transonic turbulent flow over a bump," *International Journal of Heat and Fluid Flow* 24, 584 (2003)

[41]   A. E. Perry and I. Marusic, "A wall-wake model for the turbulence structure of boundary layers. Part 1. Extension of the attached eddy hypothesis," *Journal of Fluid Mechanics* 298, 361 (1995)

[42]   F. Mathey, D. Cokljat, J. P. Bertoglio, and E. Sergent, "Assessment of the vortex method for the LES inlet conditions," *Progress in Computational Fluid Dynamics* 6, 58 (2006)

[43]   N. Jarrin, S. Benhamadouche, D. Laurence, and R. Prosser, "A synthetic eddy- method for generating inflow conditions for large-eddy simulations," *International Journal of Heat and Fluid Flow* 27, 585 (2006)

[44]   A. Spille-Kohoff and H.-J. Kaltenbach, "Generation of turbulent inflow data with a prescribed shear-stress profile," Third AFOSR International Conference on DNS/LES, Arlington, Texas, 5–9 August 2001, edited by C. Liu, L. Sakell, and T. Beutner Greyden, Columbus, OH, (2001)

[45]   Pamiès, M., Weiss, P.-E., Garnier, E., Deck, S., Sagaut, P., Generation of synthetic turbulent inflow data for large eddy simulation of spatially evolving wall-bounded flows. *Physics of Fluids* 21, 045103, 2009.

[46]   B. Roidl, M. Meinke, W. Schröder, A reformulated synthetic turbulence generation method for a zonal RANS–LES method and its application to zero-pressure gradient boundary layers, *International Journal of Heat and Fluid Flow*, Vol. 44, 2013, pp. 28-40,

[47]   J. Jeong, F. Hussain, W. Schoppa, and J. Kim, "Coherent structures near the wall in a turbulent channel flow," *Journal of Fluid Mechanics* 332, 185 (1997).

[48]   J. C. del Alamo, J. Jimenez, P. Zandonade, and R. D. Moser, "Self-similar vortex clusters in the turbulent logarithmic region," *Journal of Fluid Mechanics* 561, 329 (2006)

[49]   M. Quadrio and P. Luchini, "Integral space-time scales in turbulent wall flows," *Physics of Fluids* 15, 2219 (2003)

[50]   R. J. Adrian, C. D. Meinhart, and C. D. Tomkins, "Vortex organization in the outer region of the turbulent boundary layer," *Journal of Fluid Mechanics* 422, 1 (2000)

[51]   Smits, A.J., Dussauge, J.P., 2006. Turbulent Shear Layers in Supersonic Flow, second ed. Springer Verlag, New York.

[52]   NASA Turbulence Modeling Resource, http://turbmodels.larc.nasa.gov/index.html

[53]   Spalart, Philippe R., and Anthony Leonard. "Direct numerical simulation of equilibrium turbulent boundary layers." *Turbulent Shear Flows 5*. Springer Berlin Heidelberg, 1987. 234-252.

[54] Drela, Mark. "XFOIL: An analysis and design system for low Reynolds number airfoils." *Low Reynolds number aerodynamics*. Springer Berlin Heidelberg, 1989. 1-12.

[55] F. Farassat and G. P. Succi. The prediction of helicopter discrete frequency noise. *Vertica*, 7(4):309–320, 1983.

Appendix A

Mathematical Validation of the Synthetic Eddy Method (SEM)

A.1. Description of problem space

A finite set of points is considered $S \subset \mathbb{R}$ $S=\{x_1, x_2, ...x_s\}$ on which the synthetic velocity fluctuations are generated using SEM. An assumption is made that the mean velocity U, the Reynolds stresses R_{ij} and a characteristic length scale of the flow σ are available for the set of points considered.
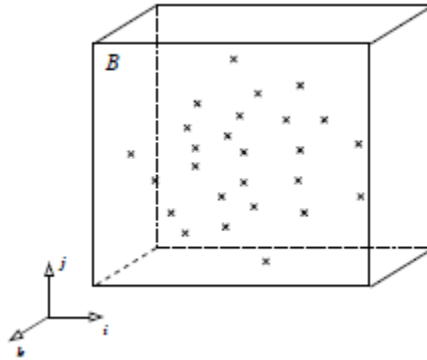

Figure A.1: The set of points on which the SEM signal is going to be computed and the surrounding box of eddies.

A box of eddies is created which contains the synthetic eddies. It is defined by

$$B = \left\{ (x_1, x_2, x_3) \in \mathbb{R}^3 : x_{i,min} < x_i < x_{i,max}, i = \{1,2,3\} \right\} \qquad (A.1)$$

where

$$x_{i,min} = \frac{\min}{x \in S}(x_i - \sigma(x)) \text{ and } x_{i,min} = \frac{\max}{x \in S}(x_i + \sigma(x)) \qquad (A.2)$$

The volume of the box of eddies is V_B. Figure A.1 shows the set of points on which the input information is available, and on which the signal will be computed, and its corresponding surrounding box of eddies B.

The velocity signal is generated by N eddies and has the following representation.

$$\boldsymbol{u} = \boldsymbol{U} + \frac{1}{\sqrt{N}} \sum_{k=1}^{N} c^k f_{\sigma(x)}(x - x^k) \qquad (A.3)$$

where the x^k are the locations of the N eddies and the c^k are the respective intensities. $f_{\sigma(x)}(x - x^k)$ is the velocity distribution of the eddy located at x^k. The differences in the distributions between the eddies depend only on the length scale σ and define f_σ by

$$f_{\sigma(x)}(x - x^k) = \sqrt{V_B}\sigma^{-3}f\left(\frac{x - x^k}{\sigma}\right)f\left(\frac{y - y^k}{\sigma}\right)f\left(\frac{z - z^k}{\sigma}\right) \qquad (A.4)$$

where the shape function is a characteristic of the distance from the wall. f has compact support in $[-\sigma, \sigma]$ and has the normalization

$$\int_{-\sigma}^{\sigma} f^2(x)dx = 1 \qquad (A.5)$$

The amplitude c^k is given by

$$c_i^k = a_{ij}\varepsilon_j^k \qquad (A.6)$$

where a_{ij} is the Cholesky decomposition of the Reynolds stress tensor

$$\begin{pmatrix} \sqrt{R_{11}} & 0 & 0 \\ \dfrac{R_{21}}{a_{11}} & \sqrt{R_{22} - a_{21}^2} & 0 \\ \dfrac{R_{31}}{a_{11}} & \dfrac{R_{32} - a_{21}a_{31}}{a_{22}} & \sqrt{R_{33} - a_{31}^2 - a_{32}^2} \end{pmatrix} \qquad (A.7)$$

and ε_j^k are independent random variables taken from any distribution with zero and unit variance. $\varepsilon_j^k \in \{-1,1\}$ with equal probability to take one value or the other. This distribution is chosen because it has a lower flatness than any other distribution.

A.2. Statistical properties of the synthesized signal

At any location x, the synthesized signal $u(x,t)$ can be seen as a random process of time. The recycling of the eddies ensures that the random variables ε_j^k and x^k remain identically distributed during the simulation. At any given time t, the position of each eddy k follows a uniform distribution over B and its intensity is either 1 or -1 with equal probability. Since the synthetic signal is a function of the random variable ε_j^k and x_i^k (which keep the same probability density function for all times), it is a stationary random process.

The mean value of the velocity signal given by equation A.3 is given by the following function

$$\langle u_i \rangle = U_i + \frac{1}{\sqrt{N}} \sum_{k=1}^{N} \langle a_{ij} \varepsilon_j^k f_{\sigma(x)}(x - x^k) \rangle \tag{A.8}$$

The random variables x_j^k and ε_j^k involved in the mean $\langle a_{ij} \varepsilon_j^k f_{\sigma(x)}(x - x^k) \rangle$ are independent thus

$$\langle a_{ij} \varepsilon_j^k f_{\sigma(x)}(x - x^k) \rangle = \langle a_{ij} \varepsilon_j^k \rangle \langle f_{\sigma(x)}(x - x^k) \rangle \tag{A.9}$$

The term $\langle a_{ij} \varepsilon_j^k \rangle$ simplifies further to $\langle a_{ij} \varepsilon_j^k \rangle = a_{ij} \langle \varepsilon_j^k \rangle = 0$ since the intensities of the eddies is either 1 or -1 with equal probability. Substituting these relations into Eq. (A.8), the mean of the velocity signal u_i is simply the input mean velocity U_i

$$\langle u_i \rangle = U_i \tag{A.10}$$

and the fluctuations u_i' around the mean velocity are

$$u_i' = \frac{1}{\sqrt{N}} \sum_{k=1}^{N} a_{ij} \varepsilon_j^k f_{\sigma(x)}(x - x^k) \tag{A.11}$$

The Reynolds stresses $\langle u_i' u_j' \rangle$ of the synthesized signal are calculated below. The linearity of the statistical mean is used to obtain.

$$\langle u_i' u_j' \rangle = \frac{1}{N} \sum_{k=1}^{N} \sum_{l=1}^{N} a_{im} a_{jn} \langle \varepsilon_m^k \varepsilon_n^l f_{\sigma(x)}(x - x^k) f_{\sigma(x)}(x - x^l) \rangle \qquad (A.12)$$

Using the independence between the positions x_j^k and the intensities ε_j^k of the eddies, Eq. A.12 becomes

$$\langle u_i' u_j' \rangle = \frac{1}{N} \sum_{k=1}^{N} \sum_{l=1}^{N} a_{im} a_{jn} \langle \varepsilon_m^k \varepsilon_n^l \rangle \langle f_{\sigma(x)}(x - x^k) f_{\sigma(x)}(x - x^l) \rangle \qquad (A.13)$$

If $k \neq l$ or $m \neq n$ the random variables ε_m^k and ε_n^l are independent and hence $\langle \varepsilon_m^k \varepsilon_n^l \rangle = \langle \varepsilon_m^k \rangle \langle \varepsilon_n^l \rangle = 0$. If $k = l$ and $m = n$, then $\langle \varepsilon_m^k \varepsilon_n^l \rangle = \langle (\varepsilon_m^k)^2 \rangle = 1$ by definition of the intensities of the eddies. Hence, we write

$$\langle \varepsilon_m^k \varepsilon_n^l \rangle = \delta_{kl} \delta_{mn} \qquad (A.14)$$

Using the above result, Eq A.13 simplifies to

$$\langle u_i' u_j' \rangle = \sum_{k=1}^{N} a_{im} a_{jm} \langle f_\sigma^2 (x - x^k) \rangle \qquad (A.15)$$

The probability density function (PDF) of x^k is needed in order to compute the mean of the quantity in Eq. (A.15). x^k follows a uniform distribution over B, hence by definition its probability density function is given by the following

$$p_1(x) = f(x) = \begin{cases} \dfrac{1}{V_B}, & if \ x \in B \\ 0, & \text{otherwise} \end{cases} \qquad (A.16)$$

Hence we have

$$I_1 = \int_{\mathbb{R}^3} p(y) f_\sigma^2 (x - y) dy = \frac{1}{V_B} \int_B f_\sigma^2 (x - y) dy \qquad (A.17)$$

Besides by definition of B,

$$x \in S, y \notin B \Rightarrow (x - y) \notin \text{supp}(f_\sigma) \qquad (A.18)$$

Hence the integral over B on Eq. A.17 can be replaced by an integral over $\mathbb{R}^3$. Using the definition of f_σ and the normalization of f, I_1 rewrites

$$I_1 = \frac{1}{V_B} \int_{\mathbb{R}^3} f_\sigma^2(x - y) dy = 1 \qquad (A.19)$$

Finally using the above result into Eq A.15 the cross correlation tensor writes

$$\langle u_i' u_j' \rangle = a_{im} a_{jm} = R_{ij} \qquad (A.20)$$

since a_{ij} is the Cholesky decomposition of R_{ij}. Hence the Reynolds stresses of the velocity fluctuations generated by SEM reproduce exactly the input Reynolds stresses R_{ij}.

Appendix B

Instructions for running the test cases

Instructions for setting up the test case (RANS)

1. The first step in the procedure is the construction of the relevant grid for the Reynolds Averaged Navier Stokes (RANS) simulation.

    a. Grid Resources can be found at the following place: http://turbmodels.larc.nasa.gov/

    b. All information is available with the use of different RANS models for the relevant grids.

    c. For the test cases presented the: flat plate zero pressure gradient and the NACA 0012 grid have been used. The modifications for the grids for conformation with the CHOPA code have been done in GridGen and Pointwise.

    d. Rules of thumbs for construction of grid:

        i. 4 points are required in the spanwise direction as CHOPA RANS model is a quasi 2-D code.

        ii. Domains need to be split for the application of the correct boundary conditions. The boundary condition files have been made available in the relevant folders.

        iii. The grid should be aligned in such a way that it conforms to (streamwise x wall normal x spanwise) (x,y,z) (This can be checked in Tecplot)

      iv. The output of GridGen should be the volumes and the file should be a *.grd file.

2. Once the RANS grid is constructed and the boundary condition file (*.bc) is obtained from GridGen direct the CHOPAGUI to the relevant *.grd and *.bc files.

    a. Follow the steps in the CHOPA manual (Chapter 2) to get the input files for CHOPA.

    b. Copy the following files: *.inp, *.grd, *.bc file to the relevant folder: (e.g. For the flat plate case the folder is E:\Bell Stuff\Test Cases\Case Files\Flat Plate Trailing Edge\Flat_Plate_RANS, while for the NACA 0012 case it is: E:\Bell Stuff\Test Cases\Case Files\NACA 0012 Trailing Edge\NACA 0012_RANS.

    c. Ensure that the executable file is present in the same folder as the above files, also make the relevant changes to the *.sh file to direct to the correct name.

    d. Ensure that the number of processors specified in the *.in, *.bc and the *.sh file are consistent.

3. You are now ready to run the RANS case. Keep track of the output file to see if the simulation is running. It should probably be run for at least 100,000 iterations to get the correct steady state results. The results can be compared to the solutions in the PSU solutions folder. Tecplot has been used to visualize the results.

Instructions for setting up the test case (NLDE)

1. The relevant fine grid needs to be constructed for use in the NLDE domain of the grid (i.e. the region near the trailing edge)

    a. The grid metrics need to be obtained using literature available on the subject (LES grids)

b. The following metrics need to be ensured: $\Delta x^+ \sim 50,100$, $\Delta y^+ < 1$, $\Delta z^+ < 20$ so that the eddies supplied by the Synthetic Eddy Method are adequately resolved.

c. The general grid configuration is 2 blocks, on each side of the body in question (i.e. Flat plate and the suction and pressure side for NACA 0012 airfoil).

d. Rules of thumbs for construction of grid:

    i. 4 points are required in the spanwise direction as CHOPA RANS model is a quasi 2-D code.

    ii. Domains need to be split for the application of the correct boundary conditions. The boundary condition files have been made available in the relevant folders.

    iii. The grid should be aligned in such a way that it conforms to (streamwise x wall normal x spanwise) (x,y,z) (This can be checked in Tecplot)

    iv. The output of GridGen should be the volumes and the file should be a *.grd file.

2. Once the NLDE grid is constructed and the boundary condition file (*.bc) is obtained from GridGen direct the CHOPAGUI to the relevant *.grd and *.bc files.

a. Follow the steps in the CHOPA manual (Chapter 2) to get the input files for CHOPA.

b. Copy the following files: *.inp, *.grd, *.bc file to the relevant folder: (e.g. For the flat plate case the folder is E:\Bell Stuff\Test Cases\Case Files\Flat Plate Trailing Edge\Flat_Plate_NLDE, while for the NACA 0012 case it is: E:\Bell Stuff\Test Cases\Case Files\NACA 0012 Trailing Edge\NACA 0012_NLDE.

c. Ensure that the executable file is present in the same folder as the above files, also make the relevant changes to the *.sh file to direct to the correct name.

    d. Ensure that the number of processors specified in the *.in, *.bc and the *.sh file are consistent.

3. Copy the *.g file from you RANS case solution folder along with the *.q file you are using to get your base flow, to the NLDE case folder.

4. Rename the RANS solution files (*.g to *.gbase) and (*.q to *.qbase) to designate them as the relevant base flow solutions.

5. In the *.bc (boundary condition file) for the NLDE case please change the appropriate boundary condition to 73 (at the inflow plane) if you want to activate the Synthetic Eddy Method to generate the turbulent fluctuations in the flow.

6. You can generate the PSJFWH.in file to get the appropriate data for the FW-H patches using the GUI but please note the multiple grid points have to be entered manually into the file, to conform to the patches that you would like to examine the data on.

Instructions for conversion to PSU-WOPWOP

1. Once you have obtained the flow solutions from the NLDE simulation, you will have a sample folder that contains the binary flow information on the FW-H surfaces you have specified.

2. The code to convert the FWH*_node.bin file to the Patch file needed for input to PSU-WOPWOP is contained in the following place: E:\Bell Stuff\Test Cases\Conversion Code \Read_patch_data.

3. In the delare_patch.f90 file change the path of the folder in the file to direct it to the sample folder and the files there to get the relevant patches.

4. Run the program to get the Patch files in the same folder as the Conversion code (Patch data).

5. The code to converr the FWH*_q.bin file to the Loading data file needed for input to PSU-WOPWOP is contained in the following place: E:\Bell Stuff\Test Cases\Conversion Code\Read_FWH_data\Read_FWH_data

6. In the declare.f90 file change the path of the folder in the file to direct it to the sample folder and the files there to get the relevant loading data.

7. Also the path of the *_0_base.q needs to be changed in the same file.

8. Run the program to get the Loading files in the same folder as the Conversion code (Loading data)

Instructions for PSU-WOPWOP

1. Once you have obtained the Patch and loading files from the Conversion code copy these files to the WOPWOP folder.

2. Make a casefile with the correct settings by consulting the WOPWOP manual and direct the WOPWOP code to the casefile.nam.

3. You should be ready to run the PSU-WOPWOP code to obtain the noise results.

Appendix C

PSU-WOPWOP test cases

To solve the Ffowcs Williams-Hawkings equation PSU-WOPWOP uses a time-domain integral formulation developed by Farassat [55]. This formulation excludes the quadrupole term of the FW-H equation and is valid for any rigid-body surface motion. A slight modification is needed for flexible surfaces. A non-rotating permeable surface implementation is done for the particular test cases that are mentioned in this thesis. If the integration surface is permeable and at a moderate distance from the body the important quadrupole terms are accounted for by the surface integration. The CFD grid is used as the basis for the acoustic patch data surface used by PSU-WOPWOP. If the grid is too coarse, only the lowest frequencies will be captured, and aliasing of the higher-frequencies may occur.

Once the conversion has been carried out from the ADS in CHOPA to PSU-WOPWOP recognizable format the specific casefile needs to be generated. The FW-H equations formulated in PSU-WOPWOP consider the airfoil moving in a stationary medium (air in this case). Thus the appropriate velocity addition should be used in the conversion when writing the perturbations from CHOPA. Also when setting up the casefile in PSU-WOPWOP the patches need to be attached to the airfoil and should move in the direction of the airfoil at the freestream Mach number.

Listed below are the casefiles that are used for the two test cases.

C.1 Example: Flat Plate Trailing Edge casefile

&EnvironmentIn

```
  nbSourceContainers = 1
  nbObserverContainers = 1
  ASCIIOutputFlag = .true.
```

```
  OASPLdBFlag = .true.
  OASPLdBAFlag = .true.
  spectrumFlag = .true.
  SPLdBFlag = .true.
  SPLdBAFlag = .true.
  acousticPressureFlag = .true.
  pressureGradient1AFlag = .false.
  sigmaflag = .false.
  loadingNoiseSigmaFlag = .false.
  thicknessNoiseSigmaFlag = .false.
  densitySigmaFlag =.true.
  momentumSigmaFlag = .true.
  pressureSigmaFlag = .true.
  totalNoiseSigmaFlag = .true.
  normalSigmaFlag = .true.
  MachSigmaFlag = .false.
  velocitySigmaFlag =.false.
  accelerationSigmaFlag =.false.
  areaSigmaFlag =.false.
  MdotrSigmaFlag = .false.
  iblankSigmaFlag =.false.
  pressureFileName = "pressure"

  debugLevel = 12

  thicknessNoiseFlag = .true.
  loadingNoiseFlag = .true.
  totalNoiseFlag = .true.
/

&EnvironmentConstants
  rho = 1.225
  c = 343.0
/

&ObserverIn
  nt   = 1000

  !xLoc = 0.7889
  !yLoc = -1.0 !-0.03 !-1.0
  !zLoc = 0.0

  !xLoc = 0.7889
  !yLoc = 1.0 !-0.03 !-1.0
  !zLoc = 0.0

  !filename = "observergrid.inp"
  radius = 1.00
  nbTheta = 360
  nbPsi = 1
```

```
   thetaMin = 0.00
   thetaMax = 6.28318531
   psiMin = 0.000
   psiMax = 0.000

   tMin = .002851! .00001
   tMax = 0.012851!0.020431!0.042113!0.007851!.00295 !0.0001
   !tMax = 0.016851!0.009851!0.016251!.00295 !0.0001
   !nbBase = 1
 /
&CB

   translationType = "knownFunction"
   VH = -34.000, 0.0, 0.0
/
 !&ObserverIn
 ! nt   = 100
 ! xLoc = 0.7889
 ! yLoc = 1.0 !-0.03 !-1.0
 ! zLoc = 0.0
 ! tMin = .002851! .00001
 ! tMax = 0.003851!0.020431!0.042113!0.008851!.00295 !0.0001
 ! !tMax = 0.015351!0.009851!0.016251!.00295 !0.0001
 ! !nbBase = 1
 /
!&CB

   !translationType = "knownFunction"
   !VH = -34.000, 0.0, 0.0
/

&ContainerIn
  Title = "flat plate"
  !patchGeometryFile="./inputfile/constantGeometry_compact.dat"
patchGeometryFile="Patch_data_1.bin","Patch_data_2.bin","Patch_data_3.bin","Patch_data_4.
bin"
patchLoadingFile="Loading_data_1.bin","Loading_data_2.bin","Loading_data_3.bin","Loading_
data_4.bin"

!patchGeometryFile = "Patch_data_1.bin"
!patchLoadingFile="Loading_data_1.bin"

  nbBase = 1
  dTau = 5e-4
  !tauMin = 0.0
  !tauMax = 0.0
  !nTau = 1
/

&CB
```

```
  translationType = "knownFunction"
  VH = -34.000, 0.0, 0.0
/
```

C.2 Example: NACA 0012 Trailing Edge casefile

```
&EnvironmentIn

  nbSourceContainers = 1
  nbObserverContainers = 1
  ASCIIOutputFlag = .true.

  OASPLdBFlag = .true.
  OASPLdBAFlag = .true.
  spectrumFlag = .true.
  SPLdBFlag = .true.
  SPLdBAFlag = .true.
  acousticPressureFlag = .true.
  pressureGradient1AFlag = .true.
  sigmaflag = .false.
  loadingNoiseSigmaFlag = .false.
  thicknessNoiseSigmaFlag = .false.
  densitySigmaFlag =.false.
  momentumSigmaFlag = .false.
  pressureSigmaFlag = .false.
  totalNoiseSigmaFlag = .false.
  normalSigmaFlag = .false.
  MachSigmaFlag = .false.
  velocitySigmaFlag =.false.
  accelerationSigmaFlag =.false.
  areaSigmaFlag =.true.
  MdotrSigmaFlag = .false.
  iblankSigmaFlag =.false.
  pressureFileName = "pressure"

  debugLevel = 12

  thicknessNoiseFlag = .true.
  loadingNoiseFlag = .true.
  totalNoiseFlag = .true.
/

&EnvironmentConstants
  rho = 1.225
  c = 343.0
/

&ObserverIn
  nt   = 700
```

```
  !xLoc = 0.7889
  !yLoc = -1.0 !-0.03 !-1.0
  !zLoc = 0.0

!   xLoc = 1.0
!   yLoc = 1.0 !-0.03 !-1.0
!   zLoc = 0.0

  !filename = "observergrid.inp"
  radius = 5.00
  nbTheta = 360
  nbPsi = 1
  thetaMin = 0.00
  thetaMax = 6.28318531
  psiMin = 0.000
  psiMax = 0.000

  tMin = 0.014577 !.002851! .00001
  tMax = 0.021577 !0.07851!0.020431!0.042113!0.007851!.00295 !0.0001
  !nbBase = 1
/
 !&ObserverIn
 ! nt   = 100
 ! xLoc = 0.7889
 ! yLoc = 1.0 !-0.03 !-1.0
 ! zLoc = 0.0
 ! tMin = .002851! .00001
 ! !tMax = 0.015351!0.009851!0.016251!.00295 !0.0001
 ! !nbBase = 1

/

&ContainerIn
  Title = "NACA 0012_500_coarse"
  !patchGeometryFile="./inputfile/constantGeometry_compact.dat"
patchGeometryFile="Patch_data_NACA                0012_1.bin","Patch_data_NACA
0012_4.bin"!,"Patch_data_NACA 0012_3.bin","Patch_data_NACA 0012_4.bin"
  patchLoadingFile="Loading_data_NACA_0012_1.bin",    "Loading_data_NACA_0012_4.bin"!,
"Loading_data_NACA_0012_3.bin", "Loading_data_NACA_0012_4.bin"
  nbBase = 1
  dTau = 5e-4
  !tauMin = 0.0
  !tauMax = 0.0
  !nTau = 1
/

&CB
  translationType = "knownFunction"
  VH = -34.000, 0.0, 0.0
/
```